Hyperspectral Image Compressive Sensing Reconstruction Using Subspace-based Nonlocal Tensor Ring Decomposition

Yong Chen, Ting-Zhu Huang, Wei He, *Member, IEEE*, Naoto Yokoya, *Member, IEEE*, and Xi-Le Zhao

Abstract—**Hyperspectral image compressive sensing reconstruction (HSI-CSR) can largely reduce the high expense and low efficiency of transmitting HSI to ground stations by storing a few compressive measurements, but how to precisely reconstruct the HSI from a few compressive measurements is a challenging issue. It has been proven that considering the global spectral correlation, spatial structure, and nonlocal self-similarity priors of HSI can achieve satisfactory reconstruction performances. However, most of the existing methods cannot simultaneously capture the mentioned priors and directly design the regularization term to the HSI. In this article, we propose a novel subspace-based nonlocal tensor ring decomposition method (SNLTR) for HSI-CSR. Instead of designing the regularization of the low-rank approximation to the HSI, we assume that the HSI lies in a low-dimensional subspace. Moreover, to explore the nonlocal self-similarity and preserve the spatial structure of HSI, we introduce a nonlocal tensor ring decomposition strategy to constrain the related coefficient image, which can decrease the computational cost compared to the methods that directly employ the nonlocal regularization to HSI. Finally, a well-known alternating minimization method is designed to efficiently solve the proposed SNLTR. Extensive experimental results demonstrate that our SNLTR method can significantly outperform existing approaches for HSI-CSR.**

Index Terms—**Compressive sensing, hyperspectral image, subspace, nonlocal self-similarity, tensor ring decomposition.**

I. INTRODUCTION

IN the past few years, compressive sensing (CS) [1] theory has been developed as an efficient mechanism for hyperspectral imagery (HSI) compression [2]. The CS theory assumes that a suitably sparse signal can be accurately reconstructed by a small number of incoherent measurements. It has been indicated that if HSI possesses the sparsity characteristic in an approximate dictionary, then the HSI-CSR is theoretically possible [3]. The HSI-CSR vastly saves the cost and storage space in the imaging and transmissive process. However, it is a difficult problem to reconstruct the image from a small number of measurements since the CS problem

Y. Chen, T.-Z. Huang and X.-L. Zhao are with School of Mathematical Sciences/Research Center for Image and Vision Computing, University of Electronic Science and Technology of China, Chengdu, Sichuan, 611731, P. R. China (e-mail: chenyong1872008@163.com, tingzhuhuang@126.com, xlzhao122003@163.com).

W. He and N. Yokoya are with Geoinformatics Unit, RIKEN Center for Advanced Intelligence Project, RIKEN, Tokyo 103-0027, Japan (e-mail: wei.he@riken.jp, naoto.yokoya@riken.jp).

is an ill-posed issue. Regularization methods are generally employed to solve this problem by introducing the prior information of the desired object. Therefore, traditional sparse regularization methods can be employed for HSI-CSR, such as ℓ_0, ℓ_1, and ℓ_p ($0 < p < 1$) sparse terms on a given dictionary (e.g., endmember dictionary [4] or wavelets [5]). Following the line of sparse representation methods, Zhang *et al.* [6] proposed a weighted Laplace prior to describe the distribution of structured sparsity for HSI-CSR. Subsequently, to promote structured sparsity, Zhang *et al.* [3] again developed a sparse representation of HSI in a data-adaptive dictionary framework. In addition, there are other sparsity-based approaches for solving the HSI-CSR problem, including spatial-spectral redundancy structure [7], joint group sparse PCA [8], and total variation (TV) regularization [9], [10]. However, these methods fail to fully capture the prior knowledge of HSI, resulting in suboptimal reconstruction results. In particular, it is difficult to reconstruct the details in the case of relatively low sampling ratios [11].

Recently, motivated by HSI denoising methods, spectral correlation, spatial smoothness, and nonlocal self-similarity priors have been widely considered for the task of HSI-CSR. As the HSI is a 3-D tensor data, tensor-based models have attracted much attention for capturing the above priors. Karami *et al.* [2] applied tensor Tucker decomposition to constrain the discrete wavelet transform coefficients of spectral bands of HSI, which can simultaneously depict the spatial and spectral information in the image. Following the line of Tucker decomposition, there are many other Tucker decomposition-based methods for HSI-CSR [11]–[15]. In [12], the authors added sparse regularization to the core tensor, which can better depict the spatial-spectral correlation of HSI. To capture the nonlocal self-similarity of the image, Du *et al.* [15] employed Tucker decomposition for the process of grouping similar tensor patches to improve the spatial-spectral correlation in HSI and achieved a better HSI-CSR result. As HSI has a smooth local structure in the spatial and spectral dimensions, weighted 3-D TV regularization was incorporated into the Tucker decomposition framework for HSI-CSR [11]. Moreover, the combination of nonlocal low-rank regularization and hyper-Laplacian regularization was proposed by using the spectral consistency and nonlocal self-similarity in the spatial dimension [16], respectively.

Although these previous works can obtain satisfactory HSI-CSR results, they are subject to specific issues. The HSI has a strong correlation in the spectral dimension [17]–[19], which

is depicted by the low-rank prior. However, previous HSI-CSR methods captured the low-rank prior in the original image space by using convex or nonconvex norms and tensor decomposition, which leads to high computational costs because of a large number of bands. Based on previous HSI processing works [20], [21], this problem can be approached by projecting the original HSI into a low-dimensional subspace, and the prior HSI can be explored by regularizing the basis coefficient, which largely decreases the computational cost and enhances the spectral correlation. Moreover, previous works cannot simultaneously capture the spectral correlation, spatial smoothness, and nonlocal self-similarity characteristics. For example, in [11], the authors used Tucker decomposition and 3-D TV to explore the first two priors while ignoring the important nonlocal self-similarity prior. Xue *et al.* [16] employed the nonlocal low-rank regularization to investigate the nonlocal self-similarity prior. However, it cannot effectively consider the spectral correlation in HSI and creates a considerable computational burden by directly applying the nonlocal prior to HSI itself. Furthermore, tensor-based methods mainly employ Tucker decomposition to constrain the image [11], [15] for HSI-CSR, which cannot achieve the best approximation for a low-rank tensor [22]–[24]. Thus, previous methods can only obtain suboptimal HSI-CSR results, and the performance of HSI-CSR can be further improved by considering these deficiencies.

To address the aforementioned issues, this article proposes a subspace-based nonlocal tensor ring decomposition method (SNLTR) for HSI-CSR, which integrates both the global spectral low-rank and spatial nonlocal self-similarity characteristics of HSI. In our work, the global spectral correlation property of HSI is depicted by subspace representation rather than low-rank approximation regularization, which was effectively introduced in HSI processing, such as dimension reduction and restoration [20], [21], [25]. Under this subspace representation method, the spatial structure depiction of the original HSI can be transformed to explore the representation coefficient images. To better preserve the spatial structure for HSI-CSR, we introduce the state-of-the-art nonlocal self-similarity prior to regularizeing the coefficient images. Moreover, motivated by the performance and effectiveness of the tensor ring (TR) representation [26] compared to other tensor decompositions, the novel TR decomposition strategy is employed to describe the low-rank property of the nonlocal grouped tensor. The contributions of this article can be summarized as follows.

1) We propose a unified subspace-based representation model to simultaneously depict the global spectral correlation and spatial nonlocal self-similarity characteristics of HSI, and the reconstruction of HSI is transformed to estimate the basis subspace and representation coefficients of HSI. In particular, the global spectral correlation is captured by subspace low-rank factorization, and novel TR decomposition is employed to exploit the nonlocal self-similarity property by regularizing the representation coefficient image.

2) We analyze the superiority of TR decomposition over traditional Tucker decomposition for HSI processing and conduct a series of experimental results to demonstrate it.

3) We design an alternating minimization algorithm to solve

our SNLTR model. Experimental results on different HSI datasets under five sampling ratios demonstrate the superiority of our SNLTR compared to exiting state-of-the-art HSI-CSR methods in terms of quantitative and visual comparisons.

The rest of this article organized is as follows. Section II describes some notations and HSI-CSR framework. The proposed SNLTR method and the corresponding optimization process are introduced in Section III. Section IV illustrates the experimental results and model analysis. Finally, we conclude this article in Section V.

II. RELATED WORK

A. Notations

In this study, scalars and vectors are represented as lowercase letters (e.g., $i, I \in \mathbb{R}$) and boldface lowercase letters (e.g., $\mathbf{x} \in \mathbb{R}^I$), respectively. Boldface capital letters (e.g., $\mathbf{X} \in \mathbb{R}^{I \times J}$) and calligraphic letters (e.g., $\mathcal{X} \in \mathbb{R}^{I_1 \times I_2 \times \cdots \times I_n}$) are used to denote matrices and tensors, respectively. $\mathcal{X}(i_1, i_2, \cdots, i_n)$ or $x_{i_1 i_2 \cdots i_n}$ denotes the element value of $\mathcal{X}$ in location $(i_1, i_2, \cdots, i_n)$. Moreover, We define two types of tensor unfolding (also named matricization) expressions in this paper. The first mode-k unfolding of tensor $\mathcal{X} \in \mathbb{R}^{I_1 \times I_2 \times \cdots \times I_n}$ is defined in [27] and denoted as $\mathbf{X}_{(k)} \in \mathbb{R}^{I_k \times I_1 \cdots I_{k-1} I_{k+1} \cdots I_n}$. The second mode-$k$ unfolding of $\mathcal{X}$, which is defined in [26], is denoted as $\mathbf{X}_{<k>} \in \mathbb{R}^{I_k \times I_{k+1} \cdots I_n I_1 \cdots I_{k-1}}$. Additionally, the unfolding matrices $\mathbf{X}_{(k)}$ can be folded as a tensor along the k-mode by $\mathcal{X} = \text{fold}_k(\mathbf{X}_{(k)})$, and a similar representation is employed to the folded process of the second mode-k unfolding matrices. The tensor Frobenius norm is represented as $\|\mathcal{X}\|_F = \left(\sum_{i_1, i_2, \cdots, i_n} (x_{i_1 i_2 \cdots i_n})^2 \right)^{\frac{1}{2}}$.

B. Problem Formulation

Recently, there have been many different compressive sensing models in HSI, including optical-based compressive HSI for imaging [28]–[32], and random measurement compressive HSI for storage and transmission [11], [33]. In our work, we mainly focus on the random measurement HSI-CSR. The reason is that before the subsequent application of HSI in remote sensing society, the images captured by a satellite or an airborne sensor should be sent to a ground station on earth. Since the size of the spectral and spatial dimensions are relatively large, the storage space of the data is very high, which produces various problems of high expense and low efficiency in transmitting them to the ground stations [11]. Based on this deficiency, it is crucial to find high-efficiency strategies for HSI compression.

The problem of random measurement HSI-CSR is to reconstruct the desired HSI from a small number of compressive measurements. Given a clean HSI $\mathcal{X} \in \mathbb{R}^{M \times N \times B}$, where B is the number of spectral bands, and M and N are the spatial resolutions, then the observed compressive measurements $\mathbf{y} \in \mathbb{R}^m$ can be represented as

$$\mathbf{y} = \Psi(\mathbf{X}), \tag{1}$$

where $\mathbf{X} \in \mathbb{R}^{B \times MN}$ denotes the rearrangement form of $\mathcal{X}$, which is obtained by vectoring each band of $\mathcal{X}$ as a vector. Ψ is

the random measurement operator, and it can be represented as $\Psi = \mathbf{DFP}$, where $\mathbf{D}$ is a random downsampling operator, $\mathbf{F}$ is the Fourier transform, $\mathbf{P}$ is a random permutation operator, and the mapping of Ψ is $\mathbb{R}^{B \times MN} \to \mathbb{R}^m$, where $m = MNB * \text{SR}$ (SR is the sampling ratio). If Ψ satisfies the restricted isometry property (RIP) [1], [34], the CS theory can guarantee strict reconstruction of a compressive $\mathbf{X}$ from $\mathbf{y}$. The definition of such a compressive operator Ψ has been proven to conform to the RIP and is widely employed to solve the image CS problem [16], [33]. The goal of HSI-CSR is to recover the original $\mathbf{X}$ from the observed compressive measurements $\mathbf{y}$. It is worth noting that we chose a generator operator Ψ to introduce our proposed methods. However, the operator Ψ in our method can also be replaced with the real implementation such as coded aperture snapshot spectral imaging (CASSI) systems (as shown in the discussion).

C. Previous Work

Directly reconstructing $\mathbf{X}$ from compressive measurements $\mathbf{y}$ is an ill-posed inverse problem, and the prior information should be investigated to make the problem as well posed. Based on the prior investigation, we can formulate the HSI-CSR as follows:

$$\min_{\mathbf{X}} \frac{1}{2}\|\mathbf{y} - \Psi(\mathbf{X})\|_F^2 + \lambda J(\mathbf{X}), \qquad (2)$$

where $J(\mathbf{X})$ denotes the regularization term to explore the prior information of the HSI, and λ denotes a regularization parameter to balance the fidelity term and the regularization term.

From the linear mixture model [35], the strong correlation of HSI exists in the spectral direction, which indicates the low-rank prior of the HSI. Moreover, as mentioned in [36]–[38], the image possesses a spatial local piecewise smooth structure. Based on these two important priors, the combination of low-rank and TV regularizations was employed to solve the HSI-CSR [10]. However, the above low-rank and TV prior only capture the correlation and smoothness in the spectral and spatial dimensions, respectively. As reported in [39], the global correlation and local smoothness of HSI occur in both spatial-spectral dimensions. To simultaneously capture these priors in HSI, Wang *et al.* [11] introduced the tensor Tucker decomposition and 3-D weighted TV regularizations to describe the prior for HSI-CSR. To further explore the property of HSI, the nonlocal self-similarity prior is explored as a powerful tool for HSI processing [21], [40]. By taking full advantage of this tool, nonlocal low-rank matrix recovery was used for HSI-CSR [16].

Although previous works have well exploited the priors for HSI-CSR, several deficiencies exist. First, they only adopted a single correlation prior (global spatial-spectral correlation or nonlocal self-similarity) to reconstruct the HSI, which indicates that it can promote the performance by simultaneously considering the correlation of global spectral and nonlocal self-similarity. Second, HSI is collected over hundreds of bands, and the quantity of data is too large. Previous nonlocal-based works mainly imposed the regularization term on the HSI, which results in high computational costs. Therefore, we can

further improve the performance of HSI-CSR by remedying these deficiencies.

III. PROPOSED SUBSPACE-BASED NONLOCAL TENSOR RING DECOMPOSITION MODEL

A. Subspace Low-rank Factorization of HSI

Due to the low-rank prior of HSI in the spectral dimension, the spectral vector (each column of $\mathbf{X}$) underlies in a b-dimensional subspace with $b \ll B$ [20]. Therefore, the subspace low-rank factorization of HSI is formulated as

$$\mathbf{X} = \mathbf{EZ}, \qquad (3)$$

where $\mathbf{E} \in \mathbb{R}^{B \times b}$ denotes an orthogonal basis matrix representing the global subspace of spectral vectors. Moreover, each row of $\mathbf{Z}$ can be reshaped as an image, and it denotes a coefficient image.

The superiority of subspace representation has been proven for HSI restoration [20], [21]. Based on the subspace factorization of HSI, the exploitation of prior information for HSI can be transformed to mine the prior information for the reduced-dimensionality coefficient image (RCI) $\mathbf{Z}$. The orthogonal basis matrix $\mathbf{E}$, as mentioned in [20], can be learned by using singular value decomposition or the HySime algorithm [25] from the low-quality data. Therefore, the regularization model (2) can be rewritten as

$$\min_{\mathbf{E},\mathbf{Z}} \frac{1}{2}\|\mathbf{y} - \Psi(\mathbf{EZ})\|_F^2 + \lambda J(\mathbf{Z}), \quad s.t. \quad \mathbf{E}^T\mathbf{E} = \mathbf{I}, \qquad (4)$$

where $J(\mathbf{Z})$ is the regularization term related with to coefficient matrix $\mathbf{Z}$.

B. Subspace-based Nonlocal Tensor Ring Decomposition Model

The subspace low-rank factorization is effective in capturing the spectral correlation of HSI, and the spatial information preservation can be transformed to constrain the coefficient $\mathbf{Z}$. Thus, the key problem is how to design an approximated regularization term for the RCI $\mathbf{Z}$ in (4). There are many regularizations that can be employed to constrain the RCI $\mathbf{Z}$ because it maintains most of the characteristics with the original HSI $\mathbf{X}$. As each row of $\mathbf{Z}$ is an image, the common image priors, such as total variation [41] and framelet regularization [18], can be used to constrain it. However, verified by the results of previous works [20], [21], [42], the nonlocal self-similarity and the correlation among the coefficient image are the state-of-the-art priors for maintaining the image information. In our work, we also adopt a nonlocal strategy to regularize $\mathbf{Z}$ for HSI-CSR. Under the assumption that nonlocal similar patches have high correlations; the stacked data tensor has a low-rank characteristic. In reality, the stacked data may be degraded by noise or have error, leading to deviation from the desirable low-rank constraint. Thus, we can model the solution of the data as $\mathcal{R}_i\mathbf{Z} = \mathcal{L}_i + \mathcal{W}_i$, where $\mathcal{R}_i\mathbf{Z} \in \mathbb{R}^{p^2 \times b \times d}$ is the i-th grouped nonlocal tensor and p and d are the spatial size of the patch and the number of similar patches, respectively. $\mathcal{L}_i$ is

the low-rank tensor, and $\mathcal{W}_i$ is the noise or error. Therefore, the model (4) can be written as

$$\min_{\mathbf{E},\mathbf{Z},\mathcal{L}_i} \frac{1}{2}\|\mathbf{y} - \Psi(\mathbf{EZ})\|_F^2 + \lambda \sum_i (\frac{1}{2}\|\mathcal{R}_i\mathbf{Z} - \mathcal{L}_i\|_F^2$$
$$+ J(\mathcal{L}_i)), \quad s.t. \quad \mathbf{E}^T\mathbf{E} = \mathbf{I}, \tag{5}$$

where $J(\mathcal{L}_i)$ is the regularization used to describe the low-rank property of tensor $\mathcal{L}_i$.

The formation of $\mathcal{R}_i\mathbf{Z} \in \mathbb{R}^{p^2 \times b \times d}$ can be summarised in the following steps: 1) reshape the RCI $\mathbf{Z} \in \mathbb{R}^{b \times MN}$ as a tensor $\mathcal{Z} \in \mathbb{R}^{M \times N \times b}$, 2) divide the tensor $\mathcal{Z} \in \mathbb{R}^{M \times N \times b}$ as an overlapped patch tensor $\mathcal{Z}_i \in \mathbb{R}^{p \times p \times b}$, and 3) find d similar patches for each i-th key patch in a neighborhood area by the measure of the Euclidean distance, i.e., $\text{Dis}(\mathcal{Z}_i, \mathcal{Z}_j) = \|\mathcal{Z}_i - \mathcal{Z}_j\|_F$, where $\mathcal{Z}_j$ is a candidate patch. The smaller $\text{Dis}(\mathcal{Z}_i, \mathcal{Z}_j)$ indicates more similar of these two patches, and then it can obtain the grouped nonlocal tensor $\mathcal{R}_i\mathcal{Z} \in \mathbb{R}^{p \times p \times b \times d}$; 4) reshape the nonlocal grouped tensor as $\mathcal{R}_i\mathbf{Z} \in \mathbb{R}^{p^2 \times b \times d}$.

In the following, how to design the low-rank tensor approximation for the grouped nonlocal patch is a key problem. Since the grouped nonlocal tensor has a correlation in both spatial-spectral and nonlocal dimensions, there are many choices that can be used to constrain $\mathcal{L}_i$, such as weighted nuclear norm minimization [21], [42], low-rank tensor decomposition [43] and tensor Tucker decomposition [44]. Although the mentioned low-rank approximation methods obtain the approval results for HSI processing, there is still room for improvement of tensor low-rank approximation. In our work, we introduce a novel TR decomposition [26] to approximate the grouped nonlocal tensor $\mathcal{L}_i$. TR decomposition approximates a high-dimensional tensor by using circular multilinear products on a sequence of third-order tensor factors.

Definition 1: (TR decomposition [26]) Assume that $\mathcal{Y} \in \mathbb{R}^{I_1 \times I_2 \times \cdots \times I_n}$ is an nth-order tensor. The TR decomposition of $\mathcal{Y}$ finds n underlying core tensors $\mathcal{G} = \{\mathcal{G}^{(1)}, \mathcal{G}^{(2)}, \cdots, \mathcal{G}^{(n)}\}$, where $\mathcal{G}^{(k)} \in \mathbb{R}^{r_k \times I_k \times r_{k+1}}$, and the connection of the core tensor $\mathcal{G}$ with each elementwise of $\mathcal{Y}$ can be represented by

$$\mathcal{Y}(i_1, i_2, \cdots, i_n) = \text{Tr}(\mathbf{G}^{(1)}(i_1)\mathbf{G}^{(2)}(i_2) \cdots \mathbf{G}^{(n)}(i_n))$$
$$= \text{Tr}\left(\prod_{k=1}^{n} \mathbf{G}^{(k)}(i_k)\right), \tag{6}$$

where $\text{Tr}(\cdot)$ is the trace operation for matrices, and $\mathbf{G}^{(k)}(i_k)$ denotes the i_k lateral slice matrix of $\mathcal{G}^{(k)}$. Since $\text{Tr}(\cdot)$ is only for the square matrix, the dimensions of the first and last core in TR decomposition should satisfy $r_1 = r_{n+1}$. Based on this definition, the vector $r = [r_1, r_2, \cdots, r_n]$ is denoted as TR rank. To simplify the representation of equation (6), we denote the decomposition as $\mathcal{Y} = \Phi([\mathcal{G}])$, where $\Phi([\mathcal{G}])$ is generated by $[\mathcal{G}]$, and each element of $\Phi([\mathcal{G}])$ is calculated by (6). More details and properties of TR decomposition can be found in references [26], [45].

In the following, we investigate why we employ TR decomposition instead of traditional Tucker decomposition to approximate the grouped nonlocal tensor. Assuming that the Tucker rank of an nth-order tensor ($\mathcal{Q} \in \mathbb{R}^{I \times I \times \cdots \times I}$) is

$[R, R, \cdots, R]$, then the Tucker decomposition of this tensor can be formulated as

$$\mathcal{Q} = \mathcal{S} \times_1 \mathbf{U}_1 \times_2 \mathbf{U}_2 \cdots \times_n \mathbf{U}_n, \tag{7}$$

where $\mathbf{U}_k \in \mathbb{R}^{I \times R}$ $(k = 1, 2, \cdots, n)$ and $\mathcal{S} \in \mathbb{R}^{R \times R \times \cdots \times R}$ are factor matrices and core tensor, respectively. First, according to the definition of these two decompositions, the number of variables of Tucker decomposition is much higher than that of TR decomposition because the number of variables of TR and Tucker decomposition is nIr^2 (assume that all TR ranks are equal) and $R^n + nIR$ (the number increases exponentially following its dimensions, and in general, $r < R$), respectively. Second, from the circular dimensional permutation invariance property of TR (see Lemma 1), the factor of TR can be regarded as equivalently and circularly rotated in the trace operation, but the Tucker decomposition strategy cannot rotate the core tensor. Third, the representation framework of TR is tensor-by-tensor; thus, the original data structure can be better preserved.

Furthermore, we focus on a 3-D HSI $\mathcal{X} \in \mathbb{R}^{M \times N \times B}$ analysis to further illustrate the priority of TR representation. There are many materials in each HSI data, and the spectral vector of HSI exists in a low-dimension subspace. Based on the Tucker decomposition, factor $\mathbf{U}_3 \in \mathbb{R}^{B \times R}$ represents the learned global basis for all spectral vectors or all materials. However, factor $\mathbf{U}_3 \in \mathbb{R}^{B \times R}$ cannot separately represent the basis for each material. Compared with Tucker decomposition, TR representation can learn the factor tensor $\mathcal{G}^{(3)} \in \mathbb{R}^{r_3 \times B \times r_1}$, where r_3 and r_1 are the number of materials and the subspace dimension of each material in HSI, respectively. Therefore, TR decomposition is effective in separately learning the basis for every materials. The other dimensions of the tensor can be analyzed analogously, thus illustrating the advantage of TR over Tucker decomposition for tensor approximation.

As a result, the proposed SNLTR for HSI-CSR is presented as

$$\min_{\mathbf{E},\mathbf{Z},\mathcal{L}_i,\mathcal{G}_i} \frac{1}{2}\|\mathbf{y} - \Psi(\mathbf{EZ})\|_F^2 + \lambda \sum_i (\frac{1}{2}\|\mathcal{R}_i\mathbf{Z} - \mathcal{L}_i\|_F^2),$$
$$s.t. \quad \mathbf{E}^T\mathbf{E} = \mathbf{I}, \quad \mathcal{L}_i = \Phi([\mathcal{G}_i]). \tag{8}$$

The proposed method can effectively capture the spectral correlation by subspace factorization, and the spatial nonlocal self-similarity and the high correlation among all coefficient images can be described by nonlocal TR decomposition. Synthesizing this superiority, the proposed SNLTR can achieve better results for HSI-CSR.

C. Optimization

As the model (8) is hard to directly optimize, the alternating minimization is employed to optimize the SNLTR model. The alternating minimization scheme means that we alternatively optimize one variable while fixing the other variables. Therefore, we can iteratively optimize the following two subproblems.

1) *Nonlocal TR decomposition $\mathcal{L}_i$ and $\mathcal{G}_i$ subproblems:* We optimize these problems while fixing other variables $\mathbf{E}$ and $\mathbf{Z}$ with the following model:

$$\min_{\mathcal{L}_i, \mathcal{G}_i} \frac{1}{2} \|\mathcal{R}_i \mathbf{Z} - \mathcal{L}_i\|_F^2, \quad s.t. \quad \mathcal{L}_i = \Phi([\mathcal{G}_i]).$$

This problem can be solved in two steps. First, the TR cores $\mathcal{G}_i$ can be optimized by solving the following problem:

$$\min_{\mathcal{G}_i} \frac{1}{2} \|\mathcal{R}_i \mathbf{Z} - \Phi([\mathcal{G}_i])\|_F^2. \tag{9}$$

When we obtain the TR cores $\mathcal{G}_i$, then $\mathcal{L}_i$ is achieved by $\mathcal{L}_i = \Phi([\mathcal{G}_i])$. Obviously, the model (9) is a nonconvex problem for $\mathcal{G}_i$. To optimize the nonconvex problem effectively, we employ proximal alternating minimization (PAM) [46], [47] to solve it.

Before solving (9), we introduce the proximal operator and then transform the model (9) into its equivalent form. Then, the problem (9) is transformed as

$$\min_{\mathcal{G}_i} \frac{1}{2} \|\mathcal{R}_i \mathbf{Z} - \Phi([\mathcal{G}_i])\|_F^2 + \frac{\rho}{2} \|\mathcal{G}_i - (\mathcal{G}_i)^j\|_F^2, \tag{10}$$

where $(\mathcal{G}_i)^j$ denotes the last results of $\mathcal{G}_i$, and ρ is a positive proximal parameter. To solve problem (10), we first introduce the mathematical operation and lemma of TR decomposition.

Definition 2: (Tensor multilinear product [26]) Let $\mathcal{G}^{(k)} \in \mathbb{R}^{r_k \times I_k \times r_{k+1}}$ and $\mathcal{G}^{(k+1)} \in \mathbb{R}^{r_{k+1} \times I_{k+1} \times r_{k+2}}$ be two adjacent core tensors, and then the multilinear product between $\mathcal{G}^{(k)}$ and $\mathcal{G}^{(k+1)}$ is represented as $\mathcal{G}^{(k,k+1)}$ and formulated as

$$\mathcal{G}^{(k,k+1)}((j_k - 1)I_n + i_k) = \mathcal{G}^{(k)}(i_k)\mathcal{G}^{(k+1)}(j_k),$$

for $i_k = 1, \cdots, I_k$, $j_k = 1, \cdots, I_{k+1}$, and where $\mathcal{G}^{(k,k+1)} \in \mathbb{R}^{r_k \times I_k I_{k+1} \times r_{k+2}}$.

According to the tensor multilinear product of Definition 2, we can define the operator Φ in $\mathcal{Y} = \Phi([\mathcal{G}])$ as

$$\mathcal{Y}(i_1, i_2, \cdots, i_n) = \mathrm{Tr}([\mathcal{G}](:, i_1 + (i_2 - 1)I_1 + \cdots + (i_n - 1)I_1 I_2 \cdots I_{n-1}, :)),$$

where $[\mathcal{G}] = \prod_{k=1}^n \mathcal{G}^{(k)} = \mathcal{G}^{(1,2,\cdots,n)} \in \mathbb{R}^{r_1 \times I_1 I_2 \cdots I_n \times r_1}$ is the multilinear product of all the TR core tensors.

Lemma 1: (Circular dimensional permutation invariance [26]) For the n-order tensor $\mathcal{Y} \in \mathbb{R}^{I_1 \times I_2 \times \cdots \times I_n}$, if its TR decomposition is $\mathcal{Y} = \Phi(\{\mathcal{G}^{(1)}, \mathcal{G}^{(2)}, \cdots, \mathcal{G}^{(n)}\})$, then $\overleftarrow{\mathcal{Y}}_k \in \mathbb{R}^{I_k \times I_{k+1} \cdots \times I_n \times I_1 \times \cdots \times I_{k-1}}$ circularly shifts the dimensions of $\mathcal{Y}$ by k. Then we have the following relation

$$\overleftarrow{\mathcal{Y}}_k = \Phi(\{\mathcal{G}^{(k)}, \mathcal{G}^{(k+1)}, \cdots, \mathcal{G}^{(n)}, \mathcal{G}^{(1)}, \cdots, \mathcal{G}^{(k-1)}\}).$$

With Lemma 1, we can obtain the following equation:

$$\mathbf{Y}_{<k>} = \mathbf{G}_{(2)}^{(k)}(\mathbf{G}_{<2>}^{(\neq k)})^T, \tag{11}$$

where $\mathbf{G}_{<2>}^{(\neq k)}$ is the second mode-2 unfolding of $\mathcal{G}^{(k+1,k+2,\cdots,n,1,\cdots,k-1)} \in \mathbb{R}^{r_{k+1} \times \prod_{i=1, i \neq k}^n I_i \times r_k}$ representing a subchain tensor generated by merging all but the k-th core tensor. Based on the equality of (11), we can iteratively solve $\mathcal{G}_i^{(u)}$ via the least square problem as follows:

$$(\mathcal{G}_i^{(u)})^{j+1} = \mathrm{fold}_2((\mathcal{R}_i \mathbf{Z}_{<u>}(\mathbf{G}_{i,<2>}^{(\neq u)})^j + \rho(\mathbf{G}_{i,(2)}^{(u)})^j) \\ ((\mathbf{G}_{i,<2>}^{(\neq u)})^{j,T}(\mathbf{G}_{i,<2>}^{(\neq u)})^j + \rho\mathbf{I})^{-1}), \tag{12}$$

where $\mathbf{I}$ is the identity matrix, and $u = 1, 2, 3$. After obtaining the TR cores $\mathcal{G}_i$, $\mathcal{L}_i$ can be computed as follows:

$$\mathcal{L}_i = \Phi([\mathcal{G}_i]).$$

2) *Subspace low-rank factorization $\mathbf{E}$ and $\mathbf{Z}$ subproblems:* After achieving the low-rank TR approximation of $\mathcal{L}_i$, we solve the subspace low-rank factorization $\mathbf{E}$ and $\mathbf{Z}$ subproblems as follows:

$$\min_{\mathbf{E}, \mathbf{Z}} \frac{1}{2} \|\mathbf{y} - \Psi(\mathbf{EZ})\|_F^2 + \lambda \sum_i (\frac{1}{2} \|\mathcal{R}_i \mathbf{Z} - \mathcal{L}_i\|_F^2), \\ s.t. \quad \mathbf{E}^T \mathbf{E} = \mathbf{I}. \tag{13}$$

We use the alternating direction method of multipliers (ADMM) [48] to optimize the problem (13). The advantage of ADMM is that it can transform (13) into simple subproblems. By introducing one auxiliary variable $\mathbf{U}$, we transform (13) into an equivalent model

$$\min_{\mathbf{E}, \mathbf{Z}, \mathbf{U}} \frac{1}{2} \|\mathbf{y} - \Psi(\mathbf{U})\|_F^2 + \lambda \sum_i (\frac{1}{2} \|\mathcal{R}_i \mathbf{Z} - \mathcal{L}_i\|_F^2) + \delta_I(\mathbf{E}^T \mathbf{E}), \\ s.t. \quad \mathbf{U} = \mathbf{EZ},$$

where $\delta_I(\cdot)$ is the indicator function. Then, the corresponding augmented Lagrangian function is

$$\min_{\mathbf{E}, \mathbf{Z}, \mathbf{U}, \mathbf{W}} \frac{1}{2} \|\mathbf{y} - \Psi(\mathbf{U})\|_F^2 + \lambda \sum_i (\frac{1}{2} \|\mathcal{R}_i \mathbf{Z} - \mathcal{L}_i\|_F^2) + \\ \delta_I(\mathbf{E}^T \mathbf{E}) + <\mathbf{W}, \mathbf{U} - \mathbf{EZ}> + \frac{\beta}{2} \|\mathbf{U} - \mathbf{EZ}\|_F^2, \tag{14}$$

where β is a positive penalty parameter, and $\mathbf{W}$ is the Lagrangian multiplier. The solution of (14) includes the following subproblems:

(1) $\mathbf{E}$-subproblem: The update of $\mathbf{E}$ is formulated as follows:

$$\min_{\mathbf{E}} <\mathbf{W}, \mathbf{U} - \mathbf{EZ}> + \frac{\beta}{2} \|\mathbf{U} - \mathbf{EZ}\|_F^2 + \delta_I(\mathbf{E}^T \mathbf{E}).$$

The close-form solution is

$$\mathbf{E} = L(\mathbf{V})R(\mathbf{V})^T, \tag{15}$$

where $L(\mathbf{V})$ and $R(\mathbf{V})$ are the left and right singular matrices of the object $\mathbf{V} = (\mathbf{U} + \frac{\mathbf{W}}{\beta})\mathbf{Z}^T$, respectively [43].

(2) $\mathbf{Z}$-subproblem: The update of $\mathbf{Z}$ is formulated as follows:

$$\min_{\mathbf{Z}} \lambda \sum_i (\frac{1}{2} \|\mathcal{R}_i \mathbf{Z} - \mathcal{L}_i\|_F^2) + <\mathbf{W}, \mathbf{U} - \mathbf{EZ}> \\ + \frac{\beta}{2} \|\mathbf{U} - \mathbf{EZ}\|_F^2,$$

which is a quadratic optimization problem, and the solution of $\mathbf{Z}$ is

$$\mathbf{Z} = \mathrm{unfold}_2((\lambda \sum_i \mathcal{R}_i^T \mathcal{R}_i + \beta \mathcal{I})^{-1}(\lambda \sum_i \mathcal{R}_i^T \mathcal{L}_i + \beta \mathcal{M})), \tag{16}$$

where $\mathcal{M}$ is a 3-D tensor of reshaping $\mathbf{E}^T(\mathbf{U} + \frac{\mathbf{W}}{\beta})$.

(3) $\mathbf{U}$-subproblem: The update of $\mathbf{U}$ is formulated as follows:

$$\min_{\mathbf{U}} \frac{1}{2} \|\mathbf{y} - \Psi(\mathbf{U})\|_F^2 + <\mathbf{W}, \mathbf{U} - \mathbf{EZ}> + \frac{\beta}{2} \|\mathbf{U} - \mathbf{EZ}\|_F^2.$$

This problem is also a quadratic optimization problem, and the solution can be obtained by using the preconditioned conjugate gradient technique to the following equation

$$(\Psi^T \Psi + \beta \mathbf{I})\mathbf{U} = (\Psi^T \mathbf{y} + \beta(\mathbf{EZ} - \frac{\mathbf{W}}{\beta})). \qquad (17)$$

(4) Finally, we update the multiplier as follows:

$$\mathbf{W} = \mathbf{W} + \beta(\mathbf{U} - \mathbf{EZ}). \qquad (18)$$

In summary, the whole optimization procedure for SNLTR is summarized in Algorithm 1. It is worth noting that we update the number of subspaces in each iteration as recommended by He *et al.* [21], because it can preserve more detailed information with the increment of the iterative number.

Algorithm 1 SNLTR method for HSI-CSR

Input: Sampling operator Ψ, compressive measure $\mathbf{y}$, TR rank $r = [r_1, r_2, r_3]^T$, parameters λ, ρ, δ and β.

1: Initialize: Estimate a preprocessed HSI $\mathbf{X}$ using a standard CS method DCT. Estimate the dimension of subspace b using HySime [25], and set $b^{(0)} = b$.

2: **for** $s = 1 : S$ **do**

3:     Update subspace $b^{(s)} = b^{(s-1)} + \delta * (s - 1)$.

4:     Estimate the subspace matrix $\mathbf{E}$ and RCI $\mathbf{Z}$ via SVD on $\mathbf{X}$.

5:     **for** each key patch $\mathcal{Z}_i$ **do**

6:         Finding d similar patches to reshape tensor $\mathcal{R}_i \mathbf{Z}$.

7:         Randomly initialize TR cores $\mathcal{G}_i$.

8:         **while** not converged **do**

9:             Update $\mathcal{G}_i = \{\mathcal{G}_i^{(1)}, \mathcal{G}_i^{(2)}, \mathcal{G}_i^{(3)}\}$ alternately via (12).

10:         **end while**

11:         Update $\mathcal{L}_i = \Phi([\mathcal{G}_i])$.

12:     **end for**

13:     **while** not converged **do**

14:         update $\mathbf{E}$ via (15).

15:         update $\mathbf{Z}$ via (16).

16:         update $\mathbf{U}$ via (17).

17:         update $\mathbf{W}$ via (18).

18:     **end while**

19:     Compute reconstructed HSI $\mathbf{X} = \mathbf{EZ}$.

20: **end for**

Output: reconstructed HSI $\mathbf{X}$.

IV. EXPERIMENTAL RESULTS

To validate the effectiveness of our proposed SNLTR method, we experiment on four popular and standard HSI datasets with five different sampling ratios (SR), i.e., 0.02, 0.05, 0.1, 0.15, and 0.2. The datasets include the Columbia MSI dataset (CAVE[1]), Harvard dataset (Harvard[2]), Washington DC Mall dataset (WDC[3]), and Hyperspectral Digital Imagery

[1]http://www1.cs.columbia.edu/CAVE/databases/multispectral

[2]http://vision.seas.harvard.edu/hyperspec/download.html

[3]https://engineering.purdue.edu/~biehl/MultiSpec/hyperspectral.html

Collection Experiment Urban dataset (Urban[4]). The CAVE and Harvard datasets are from a computer version society, and the WDC and Urban are remote sensing HSI datasets. Four random measurement HSI-CSR methods are employed as baselines in our experiments, including the DCT method, joint nuclear/TV norm minimization method (JTTV) [10], joint tensor decomposition and reweighted TV regularization method (JTenRe3-DTV) [11], hyper-Laplacian regularized nonlocal low-rank matrix recovery method (HyNLRMR) [16]. Although DCT is a common CS approach, we compare it to show that the better results are because of our method and not because of the initialization. Moreover, JTTV, JTenRe3-DTV, and HyNLRMR are also based on low-rank models and are related to our method. Furthermore, to show the superiority of TR decomposition, we compare our SNLTR method with Tucker decomposition under our subspace nonlocal framework (SNLTucker). All the experiments are performed in MATLAB R2019a employing a laptop, with 32 GB RAM, an Intel (R) Core (TM) i7-8750H CPU, and @2.20.

To evaluate the performance, visual and quantitative comparisons are employed to show the results. The quantitative indices include the peak signal-to-noise ratio (PSNR), structure similarity (SSIM) [49], feature similarity (FSIM) [50] and spectral angle mapper (SAM) [51]. The first two indices are objective assessments for image reconstruction. FSIM is used to describe the perceptual consistency with the clean image. SAM is used to evaluate the spectral distortion. Generally, larger values of PSNR, SSIM, and FSIM represent better reconstruction performance. In contrast, a smaller SAM indicates better performance of spectral information preservation.

A. Results on the CAVE dataset

There are 32 scenes in the CAVE dataset, and each scene contains 512×512 pixels with 31 spectral bands. In this dataset, we select four different scenes (Toy, Balloons, Feathers, and Painting) in which the subimages with a size of $300 \times 300 \times 31$ are extracted for testing. We present two representative cases to show the visual reconstructed comparison.

Fig. 1 and Fig. 2 show the reconstructed images and errors (the difference between the original image and the reconstructed image) of different comparison methods under $SR = 0.05$ on the Toy and Feathers scenes. We find that all test methods can well reconstruct the spatial structure. However, DCT cannot preserve the image details, which can be found in the enlarged box shown in Figs. 1(a) and 2(a). Moreover, the reconstructed image is smoothed by the JTTV method, as shown in Figs. 1(b) and 2(b). HyNLRMR obtains some artificial information under a low sampling ratio. By comparing the results of all methods, we find that the subspace-based methods SNLTucker and SNLTR achieve the best results. From Figs.1(f) and 2(f), it is evident that our SNLTR method provides the best result in reconstructing all information of the original image. For some methods, it is difficult to find the obvious difference from the reconstructed visual results. To better show the superiority of the reconstructed results, error images can be employed for comparison. The second rows of

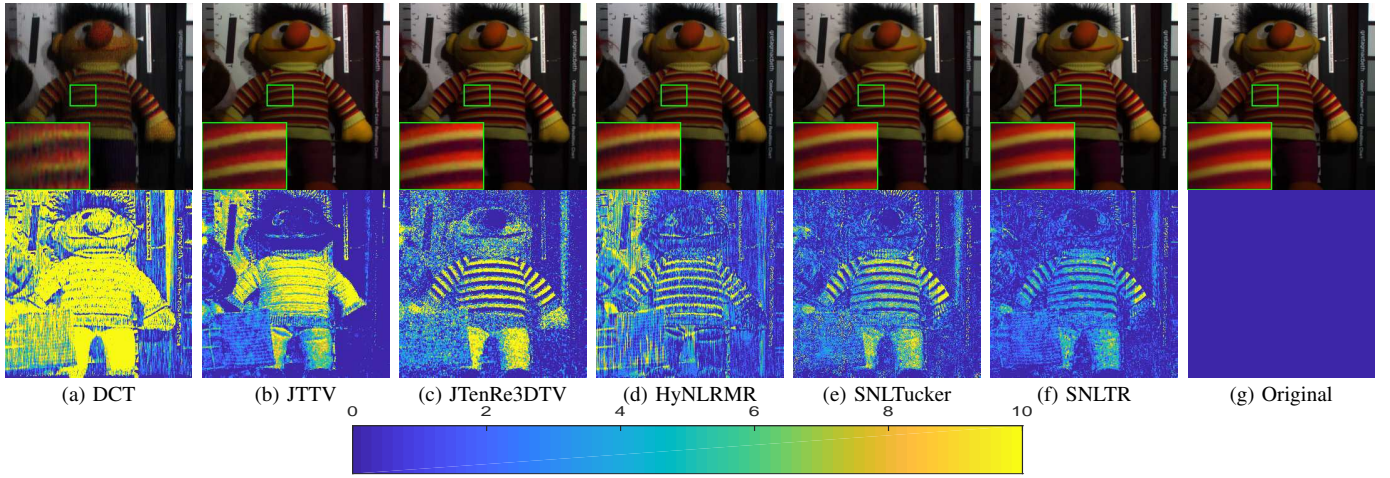[4]http://www.tec.army.mil/hypercube

Fig. 1. The first and second rows are the false-color reconstructed images (composed of bands 31, 20, 10) and error images of the competing methods under $SR = 0.05$ on the Toy dataset.
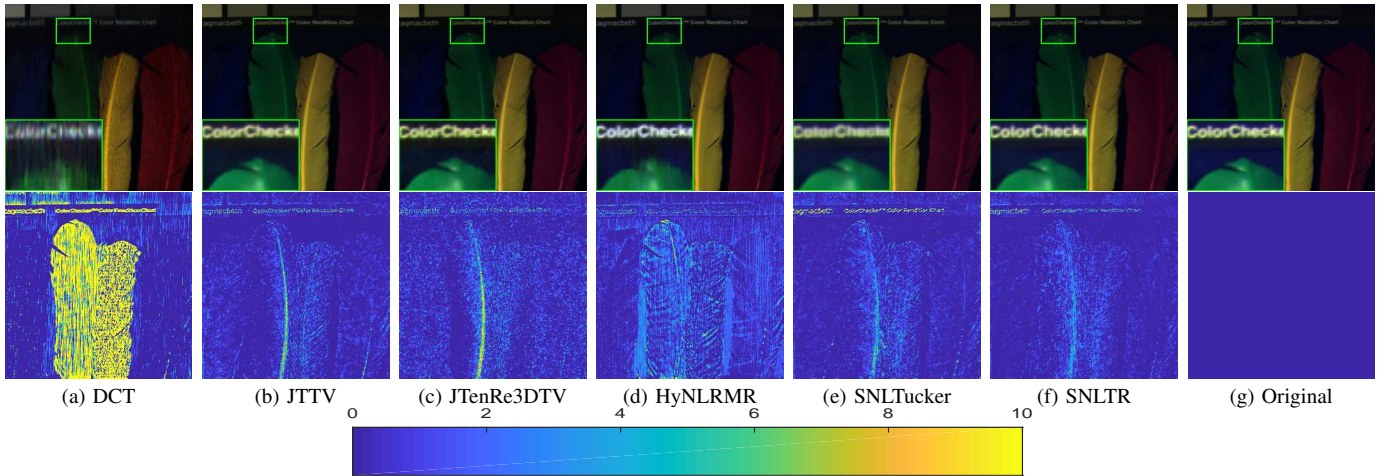

Fig. 2. The first and second rows are the false-color reconstructed images (composed of bands 22, 14, 1) and error images of the competing methods under $SR = 0.05$ on the Feathers dataset.

Fig. 1 and Fig. 2 presents the error results of all methods. From the results, we find that the subspace-based method obtains smaller error results, which again demonstrates the superiority of the subspace-based method over the methods that directly employ priors to the original image. Furthermore, by comparing the results of SNLTucker and SNLTR, we can see that SNLTR obtains better results than SNLTucker because SNLTR achieves a smaller error, which also illustrates the advantage of TR compared to traditional Tucker decomposition.

Table I lists the quantitative results of all test methods under the five sampling ratios for the CAVE dataset reconstruction, which is obtained by averaging the four scenes for each sampling ratio. The best results are highlighted in bold. From the table, our SNLTR achieves an obvious improvement over other methods except for *SR = 0.02*. Specifically, our TR decomposition can significantly outperform the Tucker decomposition method with respect to all quantitative results when SR is larger than 0.02, which illustrates the superiority of TR decomposition over Tucker decomposition. Fig. 3 presents the PSNR values on the average of four datasets for each band. It is clear that the proposed SNLTR can achieve much higher

PSNR values compared to other methods for all bands on $SR = \{0.05, 0.1, 0.15, 0.2\}$, indicating the robustness of our method for the improvement of CS reconstruction. The SAM values in Table I reflect the superiority of our SNLTR method for preserving the spectrum signature after HSI-CSR in most cases. Fig. 4 presents the spectrum signatures of one pixel on the Toy and Feathers datasets under $SR = 0.05$ before and after reconstruction. It can also be observed that the proposed SNLTR method well preserves the spectrum signature since the reconstructed curves are close to the original curves.

B. Results on the Harvard dataset

The Harvard dataset [52] consists of 50 hyperspectral images of indoor and outdoor scenes under daylight illumination, and an additional 25 images under artificial and mixed illumination. Each image in this dataset has the same size of $1040 \times 1392 \times 31$. Since there are many images and these images are too large, we also select four different scenes (img1, imga6, imgb8, imgd3) in which subimages with the spatial size 300×300 are extracted for testing.

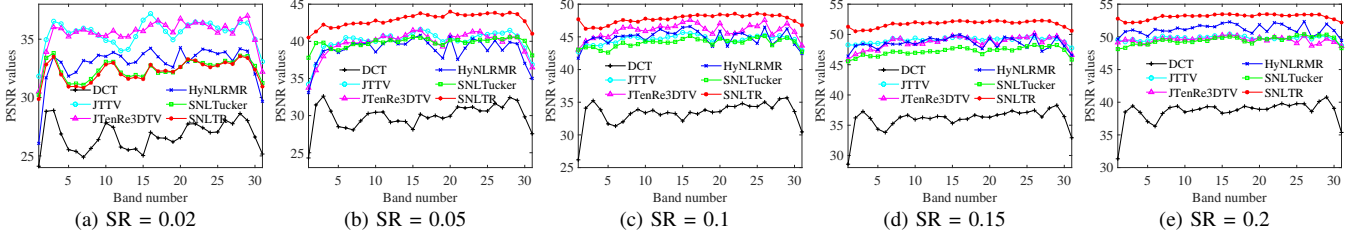Figs. 5 and 6 show the reconstructed visualizations of img1

Fig. 3. PSNR values of each band on the CAVE dataset at different sampling ratios.
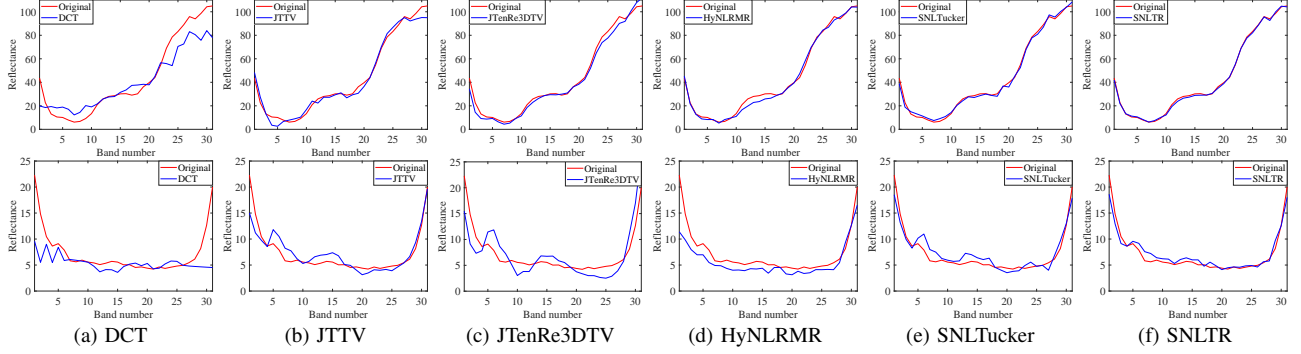

Fig. 4. Spectrum profiles of pixels in $SR = 0.05$ before and after reconstruction. Top: pixel (150, 150) on the Toy dataset. Bottom: pixel (50, 50) on the Feathers dataset.
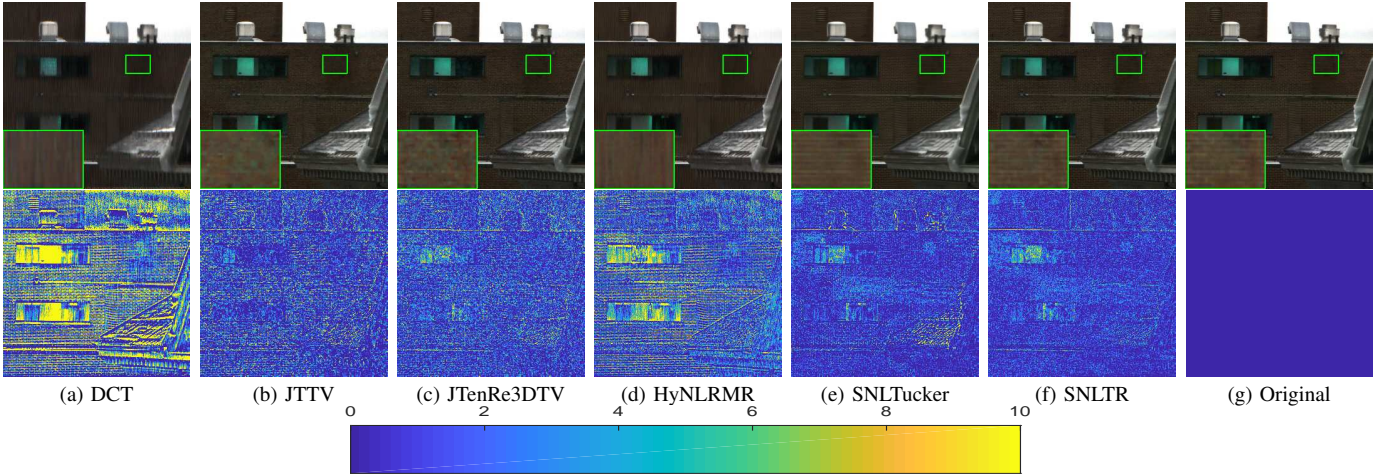

Fig. 5. The first and second rows are the false-color reconstructed images (composed of bands 30, 20, 13) and error images of the competing methods under $SR = 0.05$ on the img1 dataset.

and imga6 scenes under $SR = 0.05$, respectively. As a display, DCT cannot completely reconstruct the image details and structures. JTTV and JTenRe3DTV recover the main image characteristics, but the image texture part cannot be preserved well, as shown in the enlarged box. The results reconstructed by HyNLRMR create artifact information, and the image details are destroyed, such as the flower part shown in Fig. 6(d). Although SNLTucker obtains better reconstructed results compared with DCT, JTTV, JTenRe3DTV, and HyNLRMR, it slightly smooths the results displayed in the enlarged box. In contrast, either from the reconstructed or error results, SNLTR achieves the best performance, reconstructing and preserving the image details and textures.

Table II lists the quantitative results of five different sampling ratios on the Harvard dataset. We can observe the results corresponding to the CAVE dataset in which the SNLTR

method obtains the better results in terms of PSNR, SSIM, FSIM, and SAM in the last four sampling ratios. Fig. 7 plots the PSNR value of each band for the Harvard dataset, and it is easy to see that our SNLTR method achieves higher values in most bands except for $SR = 0.02$. The spectrum profiles of pixels on img1 and imga6 under $SR = 0.05$ are presented in Fig. 8. The subspace nonlocal tensor decomposition framework-based methods SNLTucker and SNLTR achieve satisfactory spectrum preservation compared to the other approaches.

C. Results on the WDC dataset

The Washington DC Mall dataset is selected as the third dataset for HSI-CSR experiments. This dataset was collected by the Hyperspectral Digital Imagery Collection Experiment (HYDICE), and the original size is $1208 \times 307 \times 191$. In our

This article has been accepted for publication in a future issue of this journal, but has not been fully edited. Content may change prior to final publication. Citation information: DOI 10.1109/TIP.2020.2994411, IEEE Transactions on Image Processing
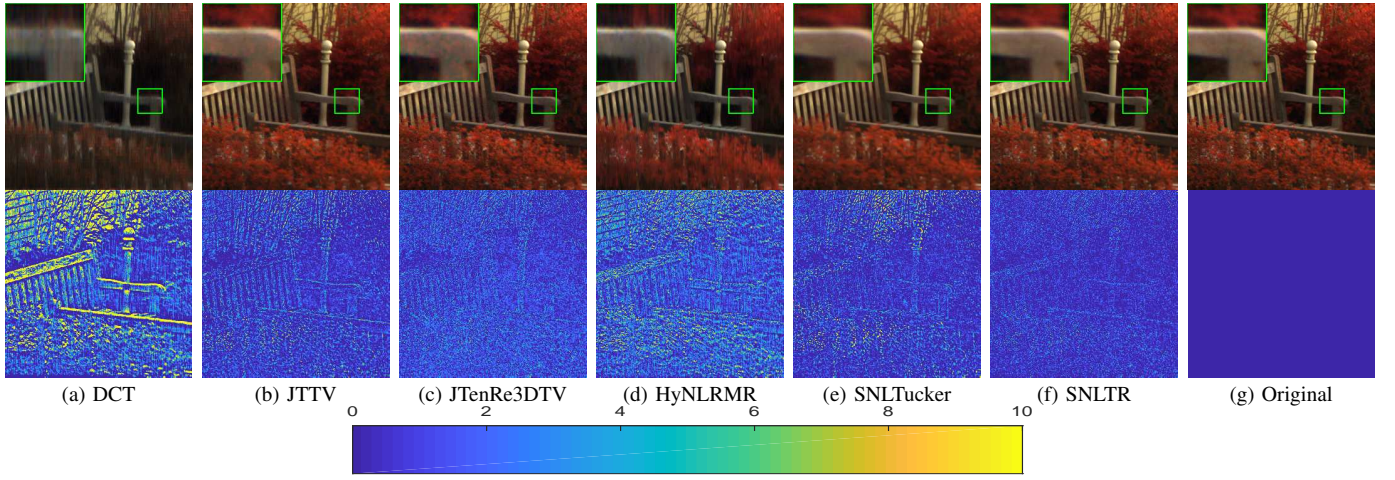
9

Fig. 6. The first and second rows are the false-color reconstructed images (composed of bands 31, 21, 7) and error images of the competing methods under $SR = 0.05$ on the imga6 dataset.
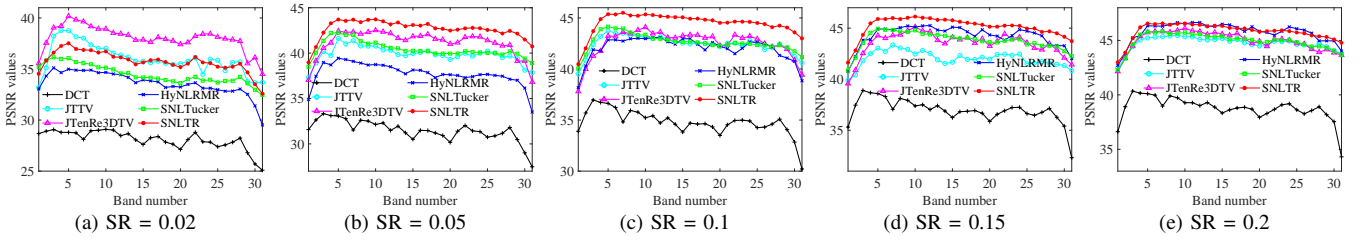

Fig. 7. PSNR values of each band on the Harvard dataset at different sampling ratios.
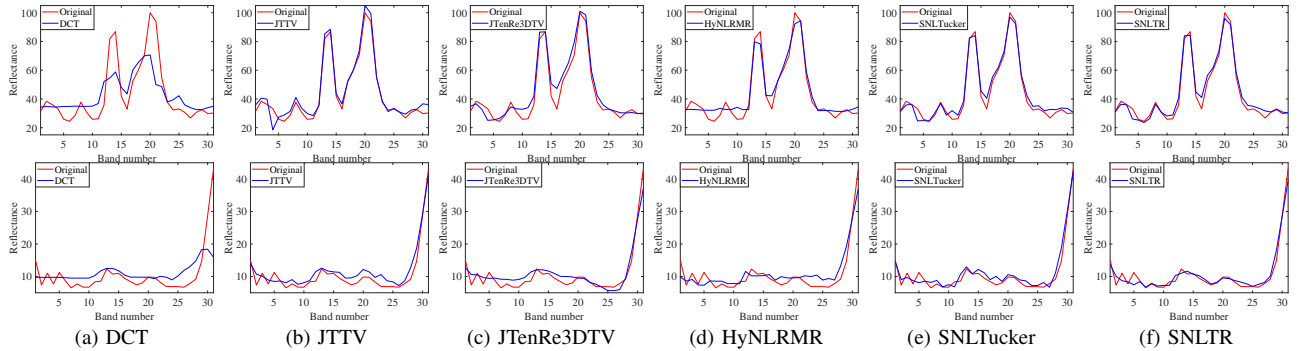

Fig. 8. Spectrum profiles of pixels in $SR = 0.05$ before and after reconstruction. Top: pixel (100, 70) on the img1 dataset. Bottom: pixel (100, 50) on the imga6 dataset.

experiment, we extract a subimage with a size of $256 \times 256 \times 191$ for testing. We also test five sampling ratios to present the results of all methods.

Fig. 9 presents the reconstructed results of $SR = 0.05$ on the WDC dataset. DCT fails to reconstruct the image structure and blurs the image details. Although JTTV, JTenRe3DTV, HyNLRMR, and SNLTucker present satisfactory visual results, they obtain worse error images compared to our SNLTR method. Moreover, as shown in the enlarged box, HyNLRMR generally changes the image contrast, and the image structure is blurred by TV-based methods JTTV and JTenRe3DTV. In summary, combining the reconstructed and error images, we can conclude that our SNLTR achieves superior results compared to other methods on the WDC dataset.

Table III presents the quantitative indices of five different sampling ratios on the WDC dataset. HyNLRMR can obtain

satisfactory results in high sampling ratios, but poor results are shown in the low sampling ratios, which indicates the instability of this method. From the results, we can observe that the SNLTR method achieves the best results in terms of PSNR, SSIM, FSIM, and SAM in all sampling ratio cases, indicating that our SNLTR method can not only effectively reconstruct the original spatial structure but also preserve the spectral information. Fig. 10 illustrates the PSNR value of each band for the WDC dataset, and it is evident that our SNLTR method achieves higher values than the other methods for almost every band in all sampling ratios, which shows the robustness of our method for all bands. Fig. 11 plots the spectrum profiles of pixels (100, 100) in $SR = 0.05$ before and after reconstruction on the WDC dataset. DCT and HyNLRMR cannot preserve the spectrum information in most bands, while JTTV, JTenRe3DTV, and SNLTucker slightly deviate from the
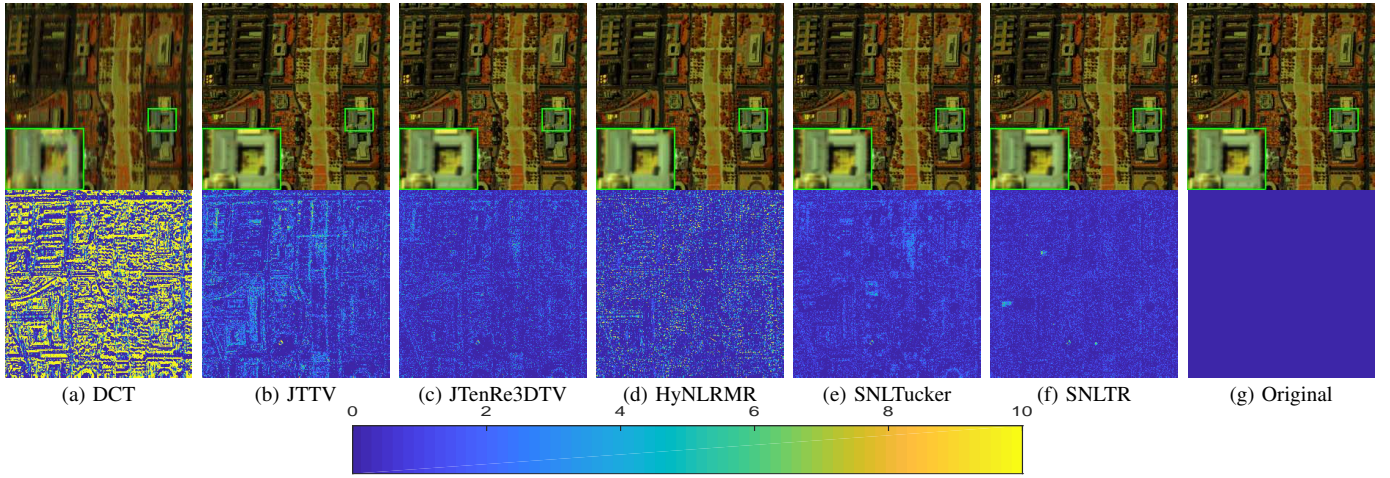
Fig. 9. The first and second rows are the false-color reconstructed images (composed of bands 65, 117, 189) and error images of the competing methods under $SR = 0.05$ on the WDC dataset.

TABLE I
QUANTITATIVE RESULTS OF ALL TEST METHODS UNDER THE FIVE SAMPLING RATIOS FOR THE CAVE DATASET RECONSTRUCTION.

SR	Index	DCT	JTTV	JTenRe3DTV	HyNLRMR	SNLTucker	SNLTR
				CAVE dataset			
0.02	PSNR	26.70	**35.53**	35.52	32.96	32.41	32.25
	SSIM	0.720	0.888	**0.896**	0.854	0.877	0.854
	FSIM	0.829	0.930	**0.933**	0.912	0.922	0.906
	SAM	0.308	**0.143**	0.162	0.221	0.185	0.195
0.05	PSNR	29.96	40.02	39.77	38.92	39.82	**42.90**
	SSIM	0.820	0.958	0.952	0.949	0.958	**0.979**
	FSIM	0.885	0.974	0.969	0.969	0.974	**0.985**
	SAM	0.248	0.094	0.111	0.113	0.094	**0.065**
0.1	PSNR	33.38	44.60	45.97	44.90	44.09	**47.75**
	SSIM	0.880	0.962	0.987	0.986	0.976	**0.990**
	FSIM	0.921	0.979	0.992	0.991	0.987	**0.994**
	SAM	0.195	0.059	0.047	0.054	0.067	**0.039**
0.15	PSNR	36.02	49.07	48.65	48.55	47.22	**51.75**
	SSIM	0.918	0.991	0.993	0.993	0.989	**0.996**
	FSIM	0.944	0.995	0.995	0.996	0.994	**0.997**
	SAM	0.157	0.034	0.037	0.037	0.046	**0.027**
0.2	PSNR	38.60	49.79	49.55	51.16	49.47	**53.08**
	SSIM	0.947	0.989	0.991	0.996	0.994	**0.997**
	FSIM	0.962	0.994	0.994	0.997	0.996	**0.998**
	SAM	0.122	0.034	0.033	0.029	0.036	**0.024**

TABLE II
QUANTITATIVE RESULTS OF ALL TEST METHODS UNDER THE FIVE SAMPLING RATIOS FOR THE HARVARD DATASET RECONSTRUCTION.

SR	Index	DCT	JTTV	JTenRe3DTV	HyNLRMR	SNLTucker	SNLTR
				Harvard dataset			
0.02	PSNR	28.08	35.99	**38.01**	33.63	34.48	35.74
	SSIM	0.731	0.878	**0.920**	0.834	0.893	0.907
	FSIM	0.857	0.914	**0.958**	0.921	0.933	0.956
	SAM	0.204	0.130	**0.104**	0.154	0.110	0.127
0.05	PSNR	31.48	39.87	41.13	37.75	40.43	**42.65**
	SSIM	0.822	0.941	0.953	0.917	0.957	**0.970**
	FSIM	0.905	0.970	0.980	0.961	0.976	**0.986**
	SAM	0.163	0.087	0.085	0.108	0.076	**0.068**
0.1	PSNR	34.78	42.44	42.51	42.04	42.62	**44.49**
	SSIM	0.881	0.963	0.964	0.967	0.971	**0.978**
	FSIM	0.941	0.984	0.986	0.985	0.986	**0.990**
	SAM	0.135	0.072	0.080	0.077	0.068	**0.061**
0.15	PSNR	36.93	42.02	43.50	44.24	43.79	**45.13**
	SSIM	0.914	0.962	0.971	0.979	0.975	**0.981**
	FSIM	0.960	0.983	0.989	0.991	0.989	**0.992**
	SAM	0.116	0.075	0.071	0.063	0.066	**0.059**
0.2	PSNR	38.75	44.74	44.97	45.76	44.94	**45.82**
	SSIM	0.937	0.979	0.980	0.983	0.981	**0.984**
	FSIM	0.972	0.991	0.992	**0.993**	0.992	0.993
	SAM	0.101	0.058	0.059	0.057	0.061	**0.056**

original curve in some bands. Moreover, the proposed SNLTR achieves a more reasonable result, approximately preserving all spectrum signature.

D. Results on the Urban dataset

In real HSI, there is some noise in the image. To test the robustness of our method for noise, we select the HYDICE urban dataset as the fourth dataset. The original size of the data is $307 \times 307 \times 210$, and we extract a subimage of size $200 \times 200 \times 184$ for testing. The removed bands are seriously contaminated by atmospheric and water absorption [53], which cannot provide useful information.

Fig. 12 shows the reconstructed images and error images of the Urban dataset under $SR = 0.05$. JTenRe3DTV and HyNLRMR blur the image structure shown in Fig. 12(c) and (d). Moreover, HyNLRMR changes the image contrast

presented in the enlarged box. DCT still cannot reconstruct the image in a low sampling ratio. JTTV, SNLTucker, and SNLTR obtain similar visual results. However, the comparison of error images illustrates the superiority of our SNLTR method. From the second row of Fig. 12, we observe that the proposed SNLTR achieves smaller errors compared with the other methods.

Table. IV lists the four evaluation indices for the Urban dataset under the five different sampling ratios. In the table, we obtain similar quantitative compared results with the WDC dataset, and the proposed SNLTR method also achieves the best results in all cases. The PSNR values over each band in all cases are presented in Fig. 12. From these results, we can observe that the proposed SNLTR outperforms all other HSI-CSR methods in PSNR values for most bands on the Urban dataset. Fig. 14 presents the spectrum profiles of pixels
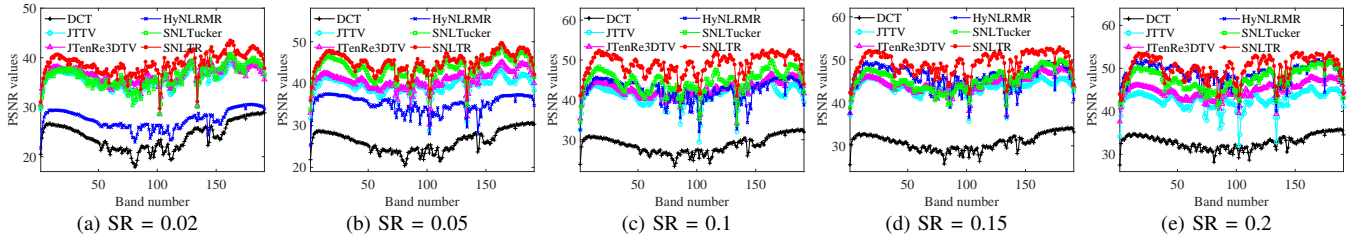
Fig. 10. PSNR values of each band on the WDC dataset at different sampling ratios.
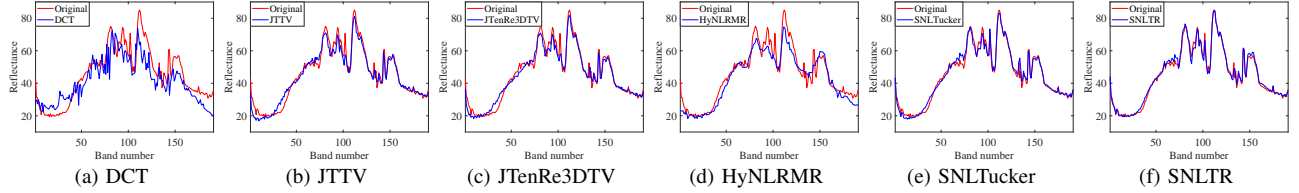

Fig. 11. Spectrum profiles of pixels (100, 100) in $SR = 0.05$ before and after reconstruction on the WDC dataset.
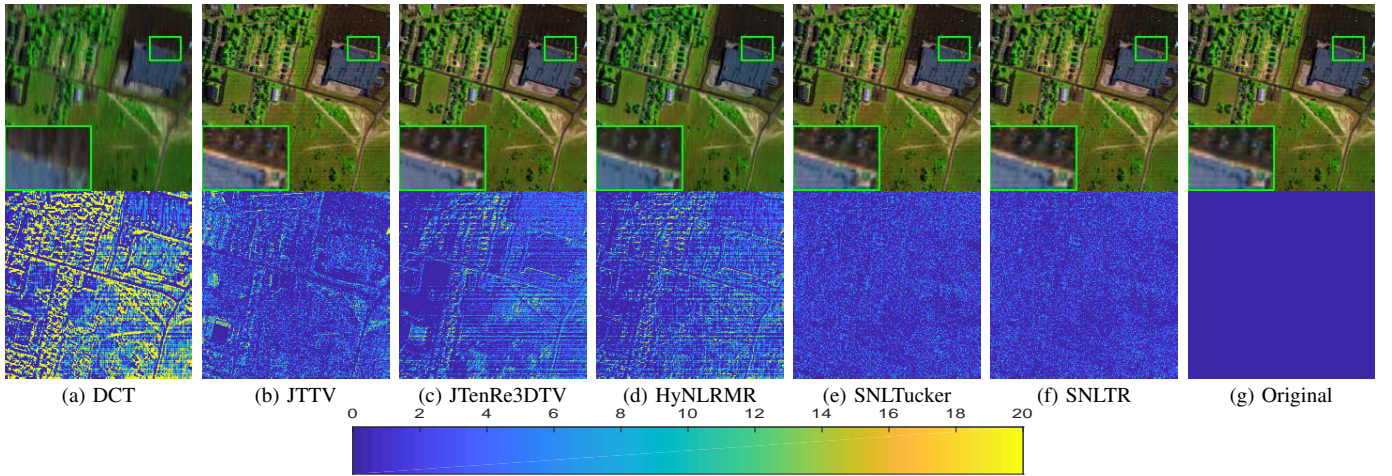

Fig. 12. The first and second rows are the false-color reconstructed images (composed of bands 132, 87, 44) and error images of the competing methods under $SR = 0.05$ on the Urban dataset.

(50, 150) in $SR = 0.05$ before and after reconstruction on the Urban dataset. SNLTR obtains the lowest error spectrum curves compared to the other methods since the reconstructed curve is closer to the original curve.

In summary, four representative datasets with different CS sampling ratios illustrate that the proposed SNLTR outperforms existing related HSI-CSR approaches by comparing the visual and quantitative results. Although our SNLTR method cannot achieve the best results in the CAVE and Harvard datasets when $SR = 0.02$, the significant improvement of our method is shown in the last two remote sensing HSI datasets (with hundreds of spectral bands) because there are only 31 bands in the CAVE and Harvard datasets; thus, the spectral correlation is not strong compared with remote sensing HSI data that have hundreds of bands. When $SR = 0.02$ in the CAVE and Harvard datasets, the observed compressive measurements are limited, which results in the low accuracy of nonlocal TR decomposition. In the case of $SR = 0.02$ in the remote sensing HSI, the subspace low-rank decomposition used to capture the high spectral correlation can help the performance of the nonlocal TR decomposition term, and the iterative estimation strategy would benefit from each other.

E. Discussion of model analysis

Before running Algorithm 1 of the SNLTR method for HSI-CSR, several related parameters should be selected, including the regularization parameter λ, proximal parameter ρ, penalty parameter β, subspace updated parameter δ, patch size p, number of nonlocal similar patches d, and TR rank $[r_1, r_2, r_3]$. Although many parameters should be adjusted, they are very robust and can be set to the same value in all experiments. We set the proximal parameter ρ to $\rho = 1$ in all experiments, and we empirically set $\beta = 0.1$ for the penalty parameter in all experiments. Moreover, the subspace update parameter is set as $\delta = 2$ in all experiments, as introduced in [21]. In the following, we analyze the sensitivity of other parameters and presernt a strategy on how it is chosen. The Toy dataset with two different sampling ratios, i.e., low sampling ratio and high sampling ratio, are adopted as the experimental cases, and we employ the PSNR index as the evaluation measure to analyze the parameter influence.

1) Regularization parameter λ: The parameter λ is employed to balance the fidelity term and the nonlocal regularization term. Fig. 15(a) shows the relationship of the parameter
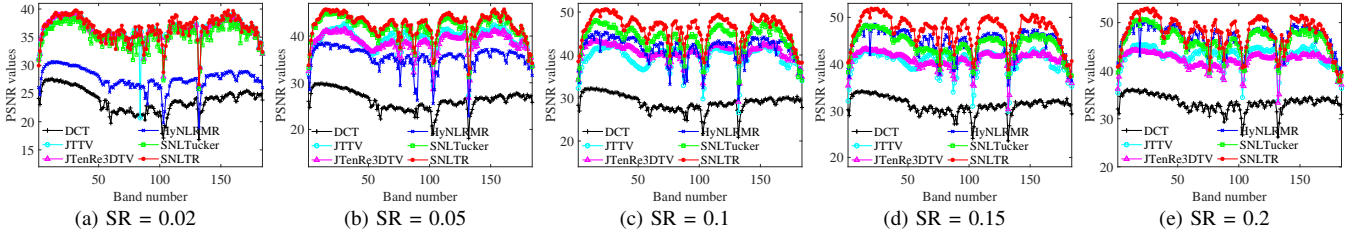
Fig. 13. PSNR values of each band on the Urban dataset at different sampling ratios.
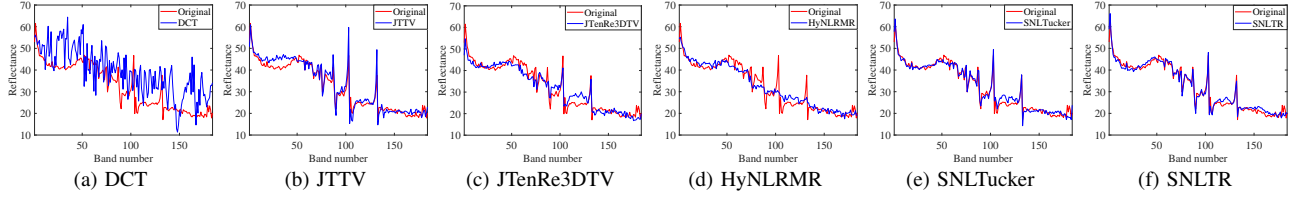

Fig. 14. Spectrum profiles of pixels (50, 150) in $SR = 0.05$ before and after reconstruction on the Urban dataset.
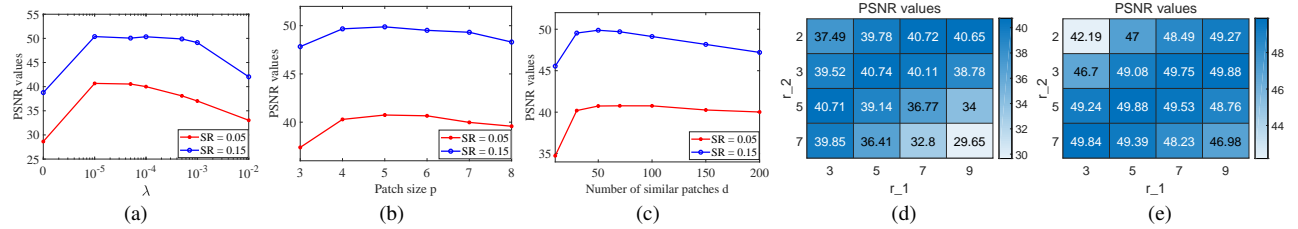

Fig. 15. The change in PSNR values with different parameter analyses at two sampling ratios. (a) λ, (b) patch size p, and (c) the number of similar patches d, (d) TR rank under $SR = 0.05$, and (e) TR rank under $SR = 0.15$.

TABLE III
QUANTITATIVE RESULTS OF ALL TEST METHODS UNDER THE FIVE
SAMPLING RATIOS FOR THE WDC DATASET RECONSTRUCTION.

SR	Index	DCT	JTTV	JTenRe3DTV	HyNLRMR	SNLTucker	SNLTR
				WDC dataset			
0.02	PSNR	24.13	35.70	36.57	27.50	36.24	**38.84**
	SSIM	0.580	0.923	0.969	0.757	0.959	**0.976**
	FSIM	0.791	0.973	0.982	0.883	0.979	**0.988**
	SAM	0.235	0.099	0.095	0.207	0.120	**0.092**
0.05	PSNR	26.23	39.51	40.78	35.11	43.75	**45.05**
	SSIM	0.705	0.969	0.987	0.946	0.993	**0.994**
	FSIM	0.853	0.990	0.993	0.974	0.996	**0.997**
	SAM	0.204	0.077	0.068	0.118	0.051	**0.049**
0.1	PSNR	28.67	41.40	42.54	42.33	44.54	**48.89**
	SSIM	0.812	0.988	0.991	0.989	0.994	**0.997**
	FSIM	0.907	0.993	0.995	0.994	0.997	**0.998**
	SAM	0.181	0.069	0.056	0.064	0.048	**0.031**
0.15	PSNR	30.78	41.68	44.54	46.06	45.31	**49.30**
	SSIM	0.876	0.980	0.994	0.995	0.995	**0.998**
	FSIM	0.938	0.994	0.997	0.998	0.997	**0.999**
	SAM	0.159	0.063	0.046	0.042	0.035	**0.027**
0.2	PSNR	32.88	42.45	44.82	48.67	47.46	**50.17**
	SSIM	0.919	0.991	0.994	0.997	0.997	**0.998**
	FSIM	0.959	0.995	0.997	**0.999**	0.998	**0.999**
	SAM	0.137	0.064	0.044	0.031	0.029	**0.025**

TABLE IV
QUANTITATIVE RESULTS OF ALL TEST METHODS UNDER THE FIVE
SAMPLING RATIOS FOR THE URBAN DATASET RECONSTRUCTION.

SR	Index	DCT	JTTV	JTenRe3DTV	HyNLRMR	SNLTucker	SNLTR
				Urban dataset			
0.02	PSNR	23.82	36.29	36.04	27.68	35.40	**36.61**
	SSIM	0.569	0.877	**0.956**	0.754	0.933	0.947
	FSIM	0.764	0.979	0.979	0.882	0.977	**0.982**
	SAM	0.210	0.083	**0.074**	0.164	0.088	0.080
0.05	PSNR	26.24	39.21	38.55	35.34	41.73	**42.43**
	SSIM	0.709	0.975	0.971	0.936	0.979	**0.982**
	FSIM	0.843	0.989	0.988	0.974	0.993	**0.994**
	SAM	0.171	0.061	0.062	0.087	0.049	**0.045**
0.1	PSNR	28.99	39.47	40.62	41.56	43.98	**46.35**
	SSIM	0.816	0.974	0.980	0.982	0.989	**0.992**
	FSIM	0.907	0.990	0.993	0.994	0.996	**0.997**
	SAM	0.139	0.061	0.049	0.049	0.038	**0.029**
0.15	PSNR	31.23	40.54	40.91	44.69	44.16	**47.44**
	SSIM	0.877	0.980	0.979	0.991	0.991	**0.995**
	FSIM	0.941	0.992	0.994	0.997	0.996	**0.998**
	SAM	0.116	0.054	0.047	0.035	0.031	**0.025**
0.2	PSNR	33.36	42.96	42.11	46.96	46.19	**48.08**
	SSIM	0.917	0.955	0.984	0.994	0.994	**0.995**
	FSIM	0.962	0.995	0.995	**0.998**	0.997	**0.998**
	SAM	0.097	0.040	0.041	0.026	0.026	**0.024**

λ with PSNR values at two different sampling ratios. The horizontal scale 0 represents our method without the nonlocal TR decomposition term. With λ larger than 0, the PSNR value achieves rapid improvement, which indicates the effectiveness of the nonlocal TR decomposition term regularization. When λ continually increases, the PSNR value exhibits a downtrend. In our work, when $SR \leq 0.1$, we empirically set $\lambda = 10^{-5}$.

$\lambda = 5 * 10^{-4}$ is fixed when $SR > 0.1$ in the experiments.

2) *Patch size p:* Fig. 15(b) presents the PSNR value with patch size p under two sampling ratios. The performance is poor when the patch size is small ($p = 3$). When the patch size is increased from 3 to 5, we observe that the PSNR obtains significant improvement. However, it shows a decrease in the PSNR value with a larger patch size. Therefore, we empirically
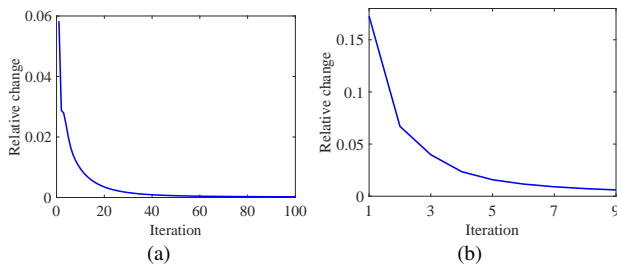
Fig. 16. Convergence analysis of the algorithm in term of relative change. (a) Inner ADMM iteration, (b) outer iteration.

fix the patch size to 5 in all experiments.

3) *The number of similar patches d:* The curve of PSNR with the number of similar patches d is presented in Fig. 15(c). We can easily see that the best results of two sampling ratios are achieved in the case of $d = 50$. Thus, the number of similar patches is empirically set to $d = 50$ in all tests.

4) *TR rank r:* The TR rank is a vital parameter for representing the correlation of the grouped tensor. There are three parameters in the TR rank, and we set the TR ranks of the spectral dimension and the nonlocal dimension the same and denote them as r_2 to simplify the analysis; then, the TR rank is set as $r = [r_1, r_2, r_2]$. Fig. 15(d) and (e) present the sensitivity analysis of PSNR with different TR ranks at $SR = 0.05$ and $SR = 0.15$, respectively. From these two figures, we find that a smaller r_2 should be selected when the sampling ratio is low. In contrast, better results are shown with a larger r_2 in the high sampling ratio. To consider the simplicity of rank selection and performance of the reconstructed results, we empirically set TR rank $r = [5, 3, 3]$ for the cases of $SR \leq 0.1$. For $SR > 0.1$, we set as $r = [5, 5, 5]$. In summary, although there are many parameters, the related parameters do not need to be manually tuned, and the proposed SNLTR can achieve better reconstruction results than other models under different sampling ratios.

5) *Computational efficiency:* Table V lists the running time of the Toy dataset under two sampling ratios. The HyNLRMR method requires the longest time since it employs the nonlocal strategy to image itself. Since our SNLTR method performs the outer iteration and nonlocal strategies while DCT, JTTV, and JTenRe3DTV only employ common spatial-spectral priors, our method requires a longer time. Although our method is not the fastest, it achieves the best-reconstructed results compared with the other methods.

6) *Convergence analysis:* Finally, we present a numerical experiment to show the convergence behavior of our method. Fig. 16 shows the curves of the relative change in $\mathbf{X}$ under $SR = 0.05$ on the Toy dataset. Since our method involves inner iterations and outer iterations, Fig. 16(a) and (b) present the convergence curves of these two iterations. From these two curves, we can find the convergent behavior of the proposed SNLTR methods.

In addition to discussing the parameter analysis of the model, the following two cases should be further discussed to illustrate the effectiveness and credibility of the proposed method. The first is the HSI-CSR performance under noisy conditions, and the other is applying our proposed framework to snapshot-

hyperspectral compressive imaging systems.

7) *HSI-CSR under different levels of noise:* To show the HSI-CSR performance of the proposed method under noisy conditions, additive Gaussian independent and identically distributed noise is added to measurements with a signal-to-noise ratio (SNR) {20 dB, 25 dB, 30 dB, 35 dB, 40 dB}. Fig. 17 presents the PSNR curves of all methods on the Toy datatset under different noise levels and different SRs. From the results, the CS-recovery performances of all methods are influenced by the low SNR. Moreover, the proposed SNLTR always provides higher PSNR values than the other methods, which indicates the robustness to noise of our method.
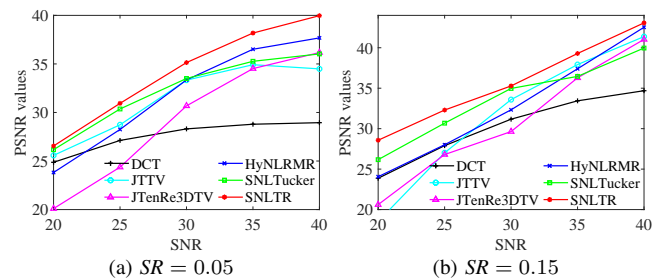
TABLE V
RUNNING TIME (IN SECONDS) OF THE TOY DATASET UNDER TWO SAMPLING RATIOS.

	Toy dataset					
SR	DCT	JTTV	JTenRe3DTV	HyNLRMR	SNLTucker	SNLTR
0.05	246.9	367.1	672.7	1861.3	875.1	1023.5
0.15	269.7	357.6	698.8	1820.5	1070.1	1410.9

Fig. 17. The change in PSNR values with different levels of noise at two sampling ratios.

8) *Snapshot compressive hyperspectral image:* In our work, we mainly focus on the random measurement compressive HSI. To extend the proposed SNLTR framework, we incorporate our method in the recovery of compressed images via CASSI [54]. The outstanding snapshot-hyperspectral compressive imaging methods GAP-TV [55] and DeSCI [54] are used for comparison. Following the same experimental setting in DeSCI, the original Toy hyperspectral image ($512 \times 512 \times 31$) is selected as the simulated experiment, and the averaged results of PSNR and SSIM are shown in Table VI. Moreover, the reconstructed images of band 18 are shown in Fig. 18. It can be seen clearly that SNLTR provides better reconstructed results than GAP-TV and DeSCI, which indicates that the proposed method can be applied to other sensing models.

TABLE VI
THE RESULTS OF PSNR AND SSIM BY DIFFERENT METHOD ON THE SIMULATED TOY DATASETS.

Method	GAP-TV	DeSCI	SNLTR
PSNR	24.66	25.91	**28.23**
SSIM	0.8608	0.9094	**0.9116**

This article has been accepted for publication in a future issue of this journal, but has not been fully edited. Content may change prior to final publication. Citation information: DOI 10.1109/TIP.2020.2994411, IEEE Transactions on Image Processing

14

(a) Original   (b) GAP-TV

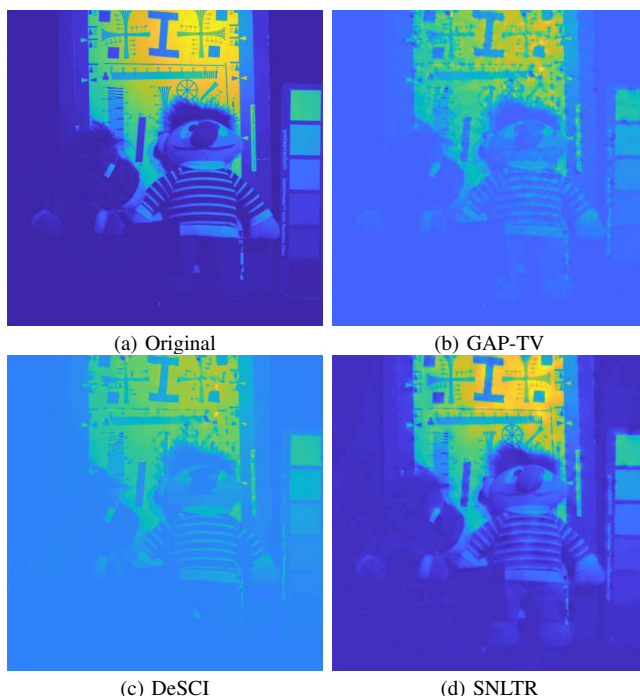(c) DeSCI   (d) SNLTR

Fig. 18. reconstructed images of band 18 of the competing methods under systems CASSI on the Toy dataset.

V. CONCLUSION

In this article, we proposed a novel subspace-based nonlocal tensor ring decomposition method for HSI-CSR. Our method integrated two important priors, i.e., global spectral low-rank and spatial nonlocal self-similarity properties, to reconstruct the original HSI from a few compressive measurements. Different from previous works that employed low-rank regularization to constrain the HSI, we enforced the spectral low-rank characterization by subspace representation. Moreover, the nonlocal self-similarity regularization of the related coefficient image was introduced to preserve the spatial structure of the reconstructed HSI, and the grouped 3-D nonlocal tensor can be effectively captured by TR decomposition. A series of experimental results were reported to illustrate that the proposed SNLTR significantly outperformed other competing approaches for HSI-CSR. In the future, we will incorporate the proposed framework into various compressive hyperspectral imaging [28]–[30] tasks to enhance its capability of HSI-CSR.

ACKNOWLEDGMENT

REFERENCES

[1] D. L. Donoho *et al.*, "Compressed sensing," *IEEE Trans. Inf. Theory*, vol. 52, no. 4, pp. 1289–1306, Apr. 2006.

[2] A. Karami, M. Yazdi, and G. Mercier, "Compression of hyperspectral images using discrete wavelet transform and tucker decomposition," *IEEE J. Sel. Top. Appl. Earth Obs. Remote Sens.*, vol. 5, no. 2, pp. 444–450, Apr. 2012.

[3] L. Zhang, W. Wei, Y. Zhang, C. Shen, A. Van Den Hengel, and Q. Shi, "Dictionary learning for promoting structured sparsity in hyperspectral compressive sensing," *IEEE Trans. Geosci. Remote Sens.*, vol. 54, no. 12, pp. 7223–7235, Dec. 2016.

[4] C. Li, T. Sun, K. F. Kelly, and Y. Zhang, "A compressive sensing and unmixing scheme for hyperspectral data processing," *IEEE Trans. Image Process.*, vol. 21, no. 3, pp. 1200–1210, Mar. 2011.

[5] M. Golbabaee and P. Vandergheynst, "Hyperspectral image compressed sensing via low-rank and joint-sparse matrix recovery," in *2012 IEEE ICASSP*. IEEE, 2012, pp. 2741–2744.

[6] L. Zhang, W. Wei, C. Tian, F. Li, and Y. Zhang, "Exploring structured sparsity by a reweighted laplace prior for hyperspectral compressive sensing," *IEEE Trans. Image Process.*, vol. 25, no. 10, pp. 4974–4988, Oct. 2016.

[7] P. Meza, I. Ortiz, E. Vera, and J. Martinez, "Compressive hyperspectral imaging recovery by spatial-spectral non-local means regularization," *Opt. express*, vol. 26, no. 6, pp. 7043–7055, 2018.

[8] Z. Khan, F. Shafait, and A. Mian, "Joint group sparse pca for compressed hyperspectral imaging," *IEEE Trans. Image Process.*, vol. 24, no. 12, pp. 4934–4942, Dec. 2015.

[9] D. T. Eason and M. Andrews, "Total variation regularization via continuation to recover compressed hyperspectral images," *IEEE Trans. Image Process.*, vol. 24, no. 1, pp. 284–293, Jan. 2014.

[10] M. Golbabaee and P. Vandergheynst, "Joint trace/tv norm minimization: A new efficient approach for spectral compressive imaging," in *19th IEEE Int. Conf. Image Process.*, Oct. 2012, pp. 933–936.

[11] Y. Wang, L. Lin, Q. Zhao, T. Yue, D. Meng, and Y. Leung, "Compressive sensing of hyperspectral images via joint tensor tucker decomposition and weighted total variation regularization," *IEEE Geosci. Remote Sens. Lett.*, vol. 14, no. 12, pp. 2457–2461, Dec. 2017.

[12] S. Yang, M. Wang, P. Li, L. Jin, B. Wu, and L. Jiao, "Compressive hyperspectral imaging via sparse tensor and nonlinear compressed sensing," *IEEE Trans. Geosci. Remote Sens.*, vol. 53, no. 11, pp. 5943–5957, Nov. 2015.

[13] L. Zhang, L. Zhang, D. Tao, X. Huang, and B. Du, "Compression of hyperspectral remote sensing images by tensor approach," *Neurocomputing*, vol. 147, pp. 358–363, Jan. 2015.

[14] J. Xue, Y. Zhao, W. Liao, and J. C.-W. Chan, "Nonlocal tensor sparse representation and low-rank regularization for hyperspectral image compressive sensing reconstruction," *Remote Sensing*, vol. 11, no. 2, p. 193, 2019.

[15] B. Du, M. Zhang, L. Zhang, R. Hu, and D. Tao, "PLTD: Patch-based low-rank tensor decomposition for hyperspectral images," *IEEE Trans. Multimedia*, vol. 19, no. 1, pp. 67–79, Jan. 2016.

[16] J. Xue, Y. Zhao, W. Liao, and J. C.-W. Chan, "Hyper-laplacian regularized nonlocal low-rank matrix recovery for hyperspectral image compressive sensing reconstruction," *Inf. Sci.*, vol. 501, pp. 406–420, Oct. 2019.

[17] W. He, H. Zhang, L. Zhang, and H. Shen, "Total-variation-regularized low-rank matrix factorization for hyperspectral image restoration," *IEEE Trans. Geosci. Remote Sens.*, vol. 54, no. 1, pp. 178–188, Jan. 2016.

[18] Y. Chen, T.-Z. Huang, X.-L. Zhao, and L.-J. Deng, "Hyperspectral image restoration using framelet-regularized low-rank nonnegative matrix factorization," *Appl. Math. Model.*, vol. 63, pp. 128–147, Nov. 2018.

[19] Y. Chen, W. He, N. Yokoya, and T. Huang, "Hyperspectral image restoration using weighted group sparsity-regularized low-rank tensor decomposition," *IEEE Trans. Cybern.*, to be published. doi: 10.1109/TCYB.2019.2936042.

[20] L. Zhuang and J. M. Bioucas-Dias, "Fast hyperspectral image denoising and inpainting based on low-rank and sparse representations," *IEEE J. Sel. Topics Appl. Earth Observ. Remote Sens.*, vol. 11, no. 3, pp. 730–742, Mar. 2018.

[21] W. He, Q. Yao, C. Li, N. Yokoya, and Q. Zhao, "Non-local meets global: An integrated paradigm for hyperspectral denoising," in *CVPR*, Jun. 2019, pp. 6868–6877.

[22] L. Yuan, J. Cao, X. Zhao, Q. Wu, and Q. Zhao, "Higher-dimension tensor completion via low-rank tensor ring decomposition," in *APSIPA ASC*. IEEE, 2018, pp. 1071–1076.

[23] Q. Zhao, M. Sugiyama, L. Yuan, and A. Cichocki, "Learning efficient tensor representations with ring-structured networks," in *ICASSP*. IEEE, 2019, pp. 8608–8612.

[24] J. Yang, X. Zhao, T. Ji, T. Ma, and T. Huang, "Low-rank tensor train for tensor robust principal component analysis," *Appl. Math. and Comput.*, vol. 367, p. 124783, 2020.

[25] J. M. Bioucas-Dias and J. M. Nascimento, "Hyperspectral subspace identification," *IEEE Trans. Geosci. Remote Sens.*, vol. 46, no. 8, pp. 2435–2445, Aug. 2008.

This article has been accepted for publication in a future issue of this journal, but has not been fully edited. Content may change prior to final publication. Citation information: DOI 10.1109/TIP.2020.2994411, IEEE Transactions on Image Processing

15

[26] Q. Zhao, G. Zhou, S. Xie, L. Zhang, and A. Cichocki, "Tensor ring decomposition," *arXiv preprint arXiv:1606.05535*, 2016.

[27] T. G. Kolda and B. W. Bader, "Tensor decompositions and applications," *SIAM Rev.*, vol. 51, no. 3, pp. 455–500, 2009.

[28] A. Wagadarikar, R. John, R. Willett, and D. Brady, "Single disperser design for coded aperture snapshot spectral imaging," *Appl. Optics*, vol. 47, no. 10, pp. B44–51, 2008.

[29] V. Saragadam and A. C. Sankaranarayanan, "KRISM — krylov subspace-based optical computing of hyperspectral images," *ACM T. Graphic.*, vol. 38, no. 5, pp. 1–14, 2019.

[30] L. Xing, Y. Liu, J. Wu, and Q. Dai, "Spatial-spectral encoded compressive hyperspectral imaging," *ACM T. Graphic.*, vol. 33, no. 6, pp. 1–11, 2014.

[31] B. Arad and O. Ben-Shahar, "Sparse recovery of hyperspectral signal from natural rgb images," *ECCV*, pp. 19–34, 2016.

[32] I. Choi, D. S. Jeon, G. Nam, D. Gutierrez, and M. H. Kim, "High-quality hyperspectral reconstruction using a spectral prior," *ACM T. Graphic.*, vol. 36, no. 6, pp. 1–13, 2017.

[33] W. Dong, G. Shi, X. Li, Y. Ma, and F. Huang, "Compressive sensing via nonlocal low-rank regularization," *IEEE Trans. Image Process.*, vol. 23, no. 8, pp. 3618–3632, Aug. 2014.

[34] E. J. Candès, J. Romberg, and T. Tao, "Robust uncertainty principles: Exact signal reconstruction from highly incomplete frequency information," *IEEE Trans. Inf. Theory*, vol. 52, no. 2, pp. 489–509, Feb. 2006.

[35] J. M. Bioucas-Dias, A. Plaza, N. Dobigeon, M. Parente, Q. Du, P. Gader, and J. Chanussot, "Hyperspectral unmixing overview: Geometrical, statistical, and sparse regression-based approaches," *IEEE J. Sel. Topics Appl. Earth Observ. Remote Sens.*, vol. 5, no. 2, pp. 354–379, Apr. 2012.

[36] Y. Chen, W. He, N. Yokoya, and T.-Z. Huang, "Blind cloud and cloud shadow removal of multitemporal images based on total variation regularized low-rank sparsity decomposition," *ISPRS J. Photogramm. Remote Sens.*, vol. 157, pp. 93–107, Nov. 2019.

[37] J.-H. Yang, X.-L. Zhao, T.-H. Ma, Y. Chen, T.-Z. Huang, and M. Ding, "Remote sensing images destriping using unidirectional hybrid total variation and nonconvex low-rank regularization," *J. Comput. Appl. Math.*, vol. 363, pp. 124–144, Jan. 2020.

[38] X.-L. Zhao, W.-H. Xu, T.-X. Jiang, Y. Wang, and M. K. Ng, "Deep plug-and-play prior for low-rank tensor completion," *Neurocomputing*, to be published. doi: https://doi.org/10.1016/j.neucom.2020.03.018.

[39] Y. Wang, J. Peng, Q. Zhao, Y. Leung, X.-L. Zhao, and D. Meng, "Hyperspectral image restoration via total variation regularized low-rank tensor decomposition," *IEEE J. Sel. Topics Appl. Earth Observ. Remote Sens.*, vol. 11, no. 4, pp. 1227–1243, Apr. 2018.

[40] Y. Chen, W. He, N. Yokoya, T.-Z. Huang, and X.-L. Zhao, "Nonlocal tensor-ring decomposition for hyperspectral image denoising," *IEEE Trans. Geosci. Remote Sens.*, vol. 58, no. 2, pp. 1348–1362, Jan. 2020.

[41] W. He, H. Zhang, and L. Zhang, "Total variation regularized reweighted sparse nonnegative matrix factorization for hyperspectral unmixing," *IEEE Trans. Geosci. Remote Sens.*, vol. 55, no. 7, pp. 3909–3921, Jul. 2017.

[42] S. Gu, L. Zhang, W. Zuo, and X. Feng, "Weighted nuclear norm minimization with application to image denoising," in *CVPR*, 2014, pp. 2862–2869.

[43] C. Cao, J. Yu, C. Zhou, K. Hu, F. Xiao, and X. Gao, "Hyperspectral image denoising via subspace-based nonlocal low-rank and sparse factorization," *IEEE J. Sel. Topics Appl. Earth Observ. Remote Sens.*, vol. 12, no. 3, pp. 973–988, Mar. 2019.

[44] Y. Peng, D. Meng, Z. Xu, C. Gao, Y. Yang, and B. Zhang, "Decomposable nonlocal tensor dictionary learning for multispectral image denoising," in *CVPR*, 2014, pp. 2949–2956.

[45] W. He, N. Yokoya, L. Yuan, and Q. Zhao, "Remote sensing image reconstruction using tensor ring completion and total variation," *IEEE Trans. Geosci. Remote Sens.*, vol. 57, no. 11, pp. 8998–9009, Jul. 2019.

[46] H. Attouch, J. Bolte, and B. F. Svaiter, "Convergence of descent methods for semi-algebraic and tame problems: proximal algorithms, forward–backward splitting, and regularized gauss–seidel methods," *Math. Program.*, vol. 137, no. 1-2, pp. 91–129, Feb. 2013.

[47] M. Razaviyayn, M. Hong, and Z.-Q. Luo, "A unified convergence analysis of block successive minimization methods for nonsmooth optimization," *SIAM J. Optim.*, vol. 23, no. 2, pp. 1126–1153, 2013.

[48] S. Boyd, N. Parikh, E. Chu, B. Peleato, J. Eckstein *et al.*, "Distributed optimization and statistical learning via the alternating direction method of multipliers," *Founda. Trends® in Mach. learn.*, vol. 3, no. 1, pp. 1–122, 2011.

[49] Z. Wang, A. C. Bovik, H. R. Sheikh, and E. P. Simoncelli, "Image quality assessment: from error visibility to structural similarity," *IEEE Trans. Image Process.*, vol. 13, no. 4, pp. 600–612, Apr. 2004.

[50] L. Zhang, L. Zhang, X. Mou, D. Zhang *et al.*, "Fsim: a feature similarity index for image quality assessment," *IEEE Trans. Image Process.*, vol. 20, no. 8, pp. 2378–2386, Aug. 2011.

[51] R. H. Yuhas, A. F. Goetz, and J. W. Boardman, "Discrimination among semi-arid landscape endmembers using the spectral angle mapper (SAM) algorithm," in *Proc. 3rd Annu. JPL Airborne Geosci. Workshop*, 1992, pp. 147–149.

[52] A. Chakrabarti and T. Zickler, "Statistics of real-world hyperspectral images," in *CVPR*, 2011, pp. 193–200.

[53] W. He, H. Zhang, and L. Zhang, "Sparsity-regularized robust nonnegative matrix factorization for hyperspectral unmixing," *IEEE J. Sel. Topics Appl. Earth Observ. Remote Sens.*, vol. 9, no. 9, pp. 4267–4279, Sep. 2016.

[54] Y. Liu, X. Yuan, J. Suo, D. Brady, and Q. Dai, "Rank minimization for snapshot compressive imaging," *IEEE Trans. Pattern Anal. Mach. Intell.*, vol. 41, no. 12, pp. 2990–3006, 2018.

[55] Y. Xin, "Generalized alternating projection based total variation minimization for compressive sensing," in *ICIP*, 2016, pp. 2539–2543.

Yong Chen received the B.S. degree in School of Science from East China University of Technology, Nanchang, China, in 2015. He is currently working toward the Ph.D. degree with the School of Mathematical Sciences, University of Electronic Science and Technology of China (UESTC), Chengdu, China.

From 2018 to 2019, he was a research intern with the Geoinformatics unit, RIKEN Center for Advanced Intelligence Project, Japan. His research interests include remote sensing image processing and low-rank matrix/tensor representation.

Ting-Zhu Huang received the B.S., M.S., and Ph.D. degrees in computational mathematics from the Department of Mathematics, Xian Jiaotong University, Xian, China.

He is currently a Professor with the School of Mathematical Sciences, University of Electronic Science and Technology of China, Chengdu, China. His research interests include scientific computation and applications, numerical algorithms for image processing, numerical linear algebra, preconditioning technologies, and matrix analysis with applications.

Prof. Huang is an Editor for the Scientific World Journal, Advances in Numerical Analysis, the Journal of Applied Mathematics, the Journal of Pure and Applied Mathematics: Advances in Applied Mathematics, and the Journal of Electronic Science and Technology, China.

Wei He (S'14-M'17) received the B.S. degree in School of Mathematics and statistics and the Ph.D degree in Surveying, Mapping and Remote Sensing (LIESMARS) from Wuhan University, Wuhan, China, in 2012 and 2017, respectively.

He is currently a researcher with the Geoinformatics unit, RIKEN Center for Advanced Intelligence Project, Japan. His research interests include image quality improvement, remote sensing image processing and low rank representation and deep learning.
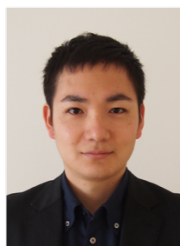
Naoto Yokoya (S'10-M'13) received the M.Eng. and Ph.D. degrees in aerospace engineering from the University of Tokyo, Tokyo, Japan, in 2010 and 2013, respectively.

He is currently a Unit Leader at the RIKEN Center for Advanced Intelligence Project, Tokyo, Japan, where he leads the Geoinformatics Unit since 2018. He is also a visiting Associate Professor at Tokyo University of Agriculture and Technology since 2019. He was an Assistant Professor at the University of Tokyo from 2013 to 2017. In 2015-2017, he was an Alexander von Humboldt Fellow, working at the German Aerospace Center (DLR), Oberpfaffenhofen, and Technical University of Munich (TUM), Munich, Germany. His research interests include image processing, data fusion, and machine learning for understanding remote sensing images, with applications to disaster management.

Dr. Yokoya won the first place in the 2017 IEEE Geoscience and Remote Sensing Society (GRSS) Data Fusion Contest organized by the Image Analysis and Data Fusion Technical Committee (IADF TC). He is an Associate Editor for the IEEE Journal of Selected Topics in Applied Earth Observations and Remote Sensing (JSTARS) since 2018. He is the Chair of IEEE GRSS IADF TC since 2019 and also the secretary of IEEE GRSS All Japan Joint Chapter since 2018.

Xi-Le Zhao received the M.S. and Ph.D. degrees from the University of Electronic Science and Technology of China (UESTC), Chengdu, China, in 2009 and 2012. He is currently a Professor with the School of Mathematical Sciences, UESTC. His research interests are model-driven and data-driven methods for image processing problems. His homepage is https://zhaoxile.github.io/.